

Chapter 2

Size Effects in Micro-scaled Plastic Deformation

2.1 Introduction

Microforming, the so-called micro-scaled plastic deformation, is to fabricate the parts or part features with the dimensions in submillimeter scale. The process has great potential to become a promising micromanufacturing method for its unique characteristics for fabrication of micro-formed parts [1]. Although a comprehensive macroforming knowledge system to support the design of process, tooling, and the metal forming part has been well established and widely used [2–6], the development of microparts by microforming, however, cannot totally be based on the traditional macroforming knowledge and the design and development paradigm of macro-formed parts as the size effect-affected deformation behaviors and process performance in microforming are different from the ones in macroforming [7–9]. In microforming, the material deformation behavior is characterized by a few grains in the deformation zone. Different properties of grains make the deformation behavior inhomogeneous and difficult to predict. In addition, there are interactive effects between workpiece size and microstructure on flow stress, flow behavior, fracture behavior, elastic recovery, and surface roughening, etc. These size effect-related deformation phenomena further affect the performance of microforming system and product quality in terms of deformation load, stability of forming system, defect formation, dimensional accuracy, surface finish, and the mechanical properties of the micro-formed parts. This chapter aims at discussing the size effect-related deformation behaviors and the newly identified phenomena, which will help understand the mechanisms and fundamentals of the size effects in microforming processes.

2.2 Flow Stress in Micro-scaled Plastic Deformation

Flow stress represents the strength of forming materials. It also determines the material deformation behaviors and deformation load in microforming processes. Flow stress affects process determination, die design, and the geometrical and

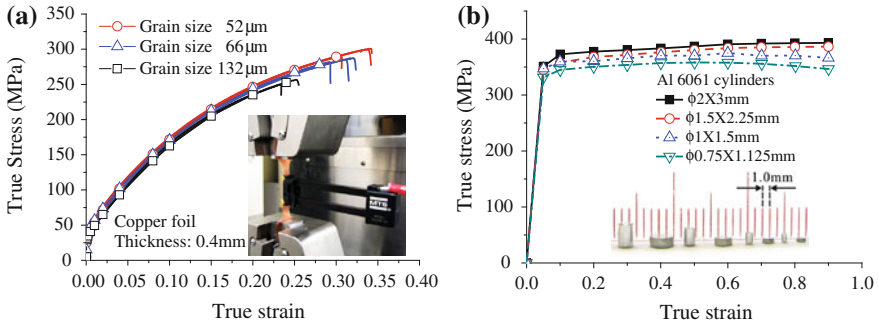


Fig. 2.1 Grain and specimen size effects on flow stress in **a** tensile and **b** compression tests [15, 16]

dimensional accuracy of micro-formed parts. In microforming arena, size effect on flow stress has been extensively investigated via compression and tensile tests using different size-scaled specimens with different grain sizes in many prior studies [8, 10–16]. The change of flow stress with the variation of specimen and grain sizes is shown in Fig. 2.1. From the figure, it can be seen that the flow stress decreases with the reduction of specimen size and the increase of grain size. The grain size effect on flow stress occurs in both the macro- and micro-sized specimens, while the specimen geometry size effect is only significant when there is less than 10 grains in the cross-section of specimen [17]. The flow stress of material has a close relationship with the characteristics of grain boundary. The specimen and grain size effects on the micro-scaled plastic deformation behavior have been investigated separately in prior studies. However, these two size effects actually interact and interplay to affect the material deformation behaviors. In this section, the change of flow stress with specimen and grain sizes is articulated. The different models proposed based on grain boundary strengthening and the influence of surface grains are discussed for providing an in-depth understanding of the size effect affected flow stress in microforming.

2.2.1 Strengthening Behavior

The material size effect on flow stress is related to the formation and movement of dislocations. It needs to generate massive dislocations in material to initiate plastic yielding and deformation. In yielding process, there are mainly three stages [18]. In the first stage, incompatible stress is generated at grain boundary due to the different elastic properties of neighboring grains, as shown in Fig. 2.2a. The grain boundary region having higher stress than that at the grain interior deforms plastically. In the second stage, the deformation of grain boundary and the generation of geometrically necessary dislocation (GND) decrease the incompatibility of stress at the grain boundary, as shown in Fig. 2.2b, c. The work-hardened grain

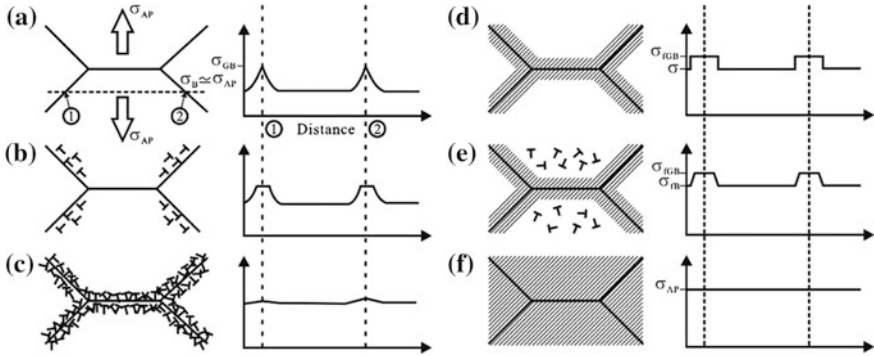


Fig. 2.2 Stages in polycrystalline deformation, starting with **a, b** localized plastic flow in grain boundary regions (microyielding), forming a work-hardened layer in grain boundary **c, d** that effectively reinforces the microstructure, and leads to **e, f** macroyielding in which the bulk of grains undergo plastic deformation [18]

boundaries act as a rigid network structure which resists the deformation of grain interior (Fig. 2.2d). In the third stage, the macro-yielding takes place as long as the applied stress is large enough to further initiate the plastic flow of grain boundary (Fig. 2.2e). The dislocation density at grain boundary and interior becomes the same and the plastic incompatibility disappears (Fig. 2.2f). The atoms at grain interior have a crystalline periodic arrangement, while the atom arrangement at grain boundary is more disordered and the characteristics of grain boundary are like the ones in amorphous material. The grain boundary increases the strength of material via blocking dislocation movement, resulting in dislocation pile-up. The work-hardening effect is actually caused by the entanglement of dislocations. The ratio of the total grain boundary surface area to material volume decreases with the decrease of specimen size and the increase of grain size [19–21]. This leads to the decrease of grain boundary strengthening effect and the flow stress.

The above explanation of size effect on flow stress is based on the conventional understanding of grain boundary strengthening behavior. Actually, there exists size effect on the dislocation formation at grain interior. Hug and Keller [22] examined the dislocation structures of the elongated nickel foils with different ratios of foil thickness to grain size (t/d). It is found that a well-defined dislocation cell structure with high dislocation density is formed for the specimen with the t/d ratio of 14, as shown in Fig. 2.3. In addition, the cells in surface grains are slightly larger than those in inner grains. For the specimen with the t/d ratio of 2.5, the dislocation cells become larger and the dislocation density decreases. The diameter of dislocation cells in the surface grains is about three times the ones in the inner grains. For the specimen with the t/d ratio of 0.125, a poorly defined cell structure is observed and the cell diameter is larger than that in the specimen with a large t/d ratio. Furthermore, the difference between the surface and inner cells is subtle. Based on the above results, Hug and Keller [22] concluded that dislocation cells exhibit a delay in their spatial arrangement for the specimen with a small t/d ratio.

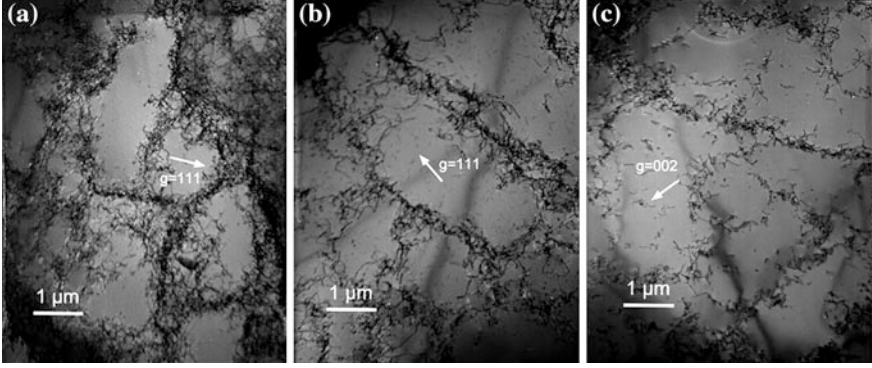


Fig. 2.3 Dislocation structure in the core of the elongated nickel foils with the different ratios of specimen size to grain size (t/d) [22]. **a** $t/d = 14$, **b** $t/d = 2.5$ and **c** $t/d = 0.125$

2.2.2 Modified Hall–Petch Relation

The most well-known empirical model for describing the grain size effect on material yield stress (σ_y) is Hall–Petch relation [23, 24] as follows:

$$\sigma_y(d) = \sigma_{hp} + K_{hp}d^{-1/2} \quad (2.1)$$

where σ_{hp} and K_{hp} are material constants. Armstrong [25] further developed Eq. (2.1) with the consideration of strain hardening into the following equation:

$$\sigma(\varepsilon, d) = \sigma_{hp}(\varepsilon) + K_{hp}(\varepsilon)d^{-1/2} \quad (2.2)$$

where $\sigma_{hp}(\varepsilon)$ and $K_{hp}(\varepsilon)$ are the functions of strain. To include the parameters of specimen and grain sizes in the material model, prior studies [20, 26–28] introduced the ratio of specimen size (D —diameter of billet, t —thickness of foil) to grain size (d) to quantify the size effect in the following.

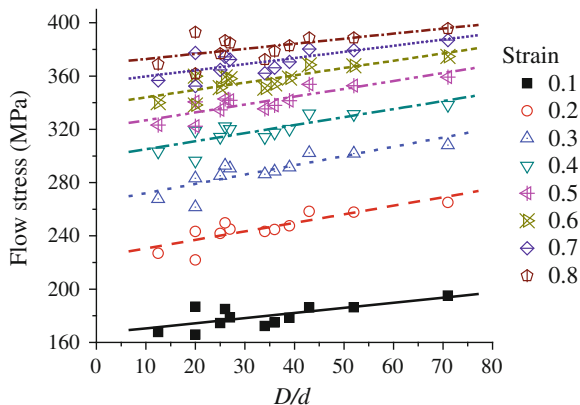
$$N = \frac{\text{Specimen size } (D, t)}{\text{Grain size } (d)} \quad (2.3)$$

It is revealed that the flow stress has a linear relationship with N for a given strain, as shown in Fig. 2.4. The relationship can be represented as:

$$\sigma(\varepsilon, N) = \sigma_n(\varepsilon) + K_n(\varepsilon)N \quad (2.4)$$

where $\sigma_n(\varepsilon)$ and $K_n(\varepsilon)$ are material constants and they are the function of strain. In Eq. (2.2), it can be seen that when the grain size (d) is large, the term $K_{hp}(\varepsilon)d^{-1/2}$ presenting the grain boundary strengthening effect becomes insignificant. The dominated term $\sigma_{hp}(\varepsilon)$ thus represents the flow stress of grain interior or coarse-grained and untextured polycrystal [29]. Equation (2.4) actually presents the similar characteristics of Eq. (2.2). When N becomes small, it results in the

Fig. 2.4 Change of flow stress with D/d [30]



domination of $\sigma_n(\varepsilon)$. Chan and Fu [30] showed that $\sigma_{np}(\varepsilon)$ varies with specimen size. Therefore, $\sigma_n(\varepsilon)$ in Eq. (2.4) provides a better description of the deformation behavior of grain interior with taking the interactive effect of specimen and grain sizes into consideration.

2.2.3 Grain Boundary Surface Area-Based Model

The material strengthening effect could be caused by the changing fraction of grain boundary, which impedes dislocation movement [18, 31]. The ratio of the internal grain boundary surface area to the total grain boundary surface area is thus introduced to quantify the interactive effects of the specimen and grain sizes on the work-hardening behavior and flow stress. To simplify the analysis, the grain geometry is considered as a cubic. The grain boundary surface area can be determined from the geometrical point of view. Figure 2.5 shows the schematic illustration for formulating the internal grain boundary surface area of a cylindrical specimen. At the top view of a quarter of specimen, the sum of horizontal lengths of grain boundaries can be expressed as

$$l_h = \sum_0^{n=f[r/g]} \sqrt{(r^2 - (ng)^2)} \quad (2.5)$$

where $f[r/g]$ is the greatest integer function. r and g are the radius of specimen and grain size, respectively. The sum of the horizontal and vertical lengths of grain boundaries shown in the top view is

$$l_{h+v} = 8 \left(\sum_0^{n=f[r/g]} \sqrt{(r^2 - (ng)^2)} \right) - 4r \quad (2.6)$$

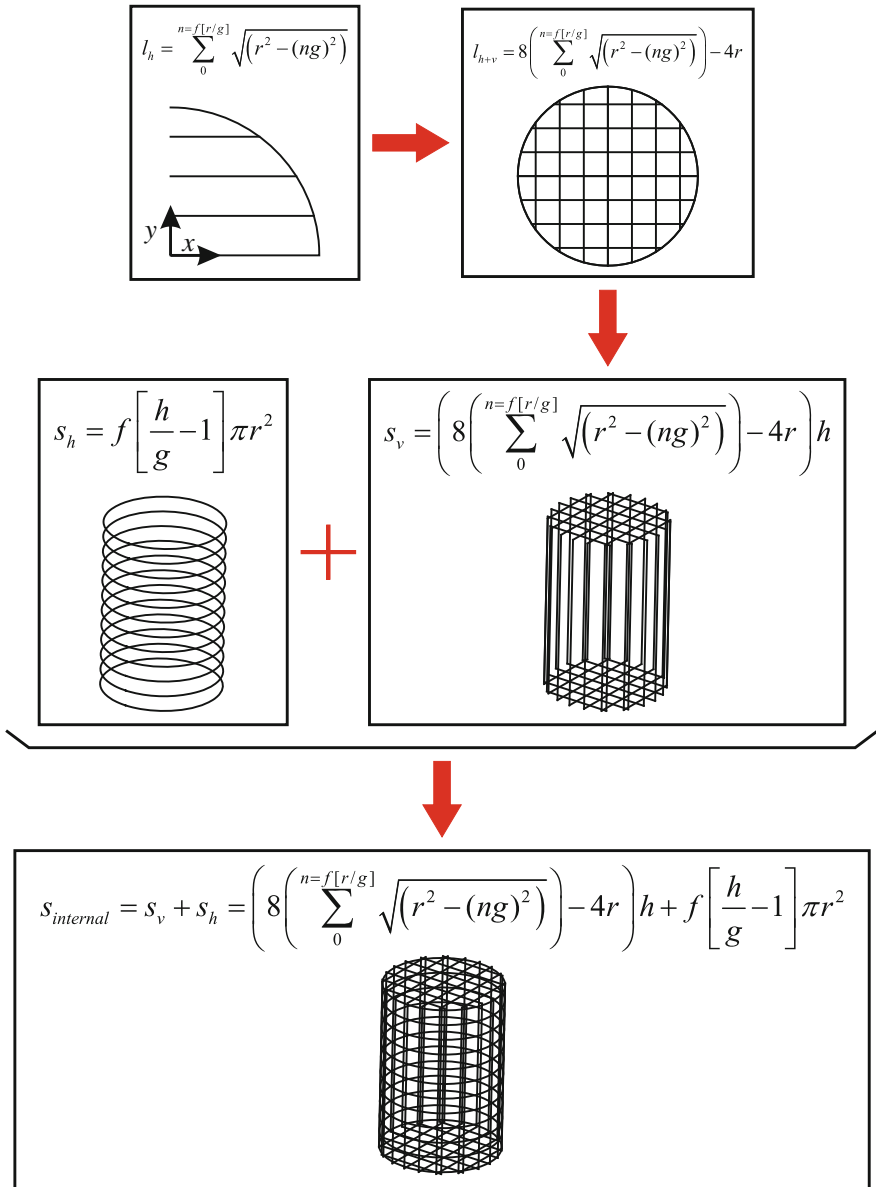


Fig. 2.5 Schematic illustration of the formulation of the internal grain boundary surface area [21]

In addition, the sum of the vertical grain boundary surface areas is determined by

$$s_v = \left(8 \left(\sum_0^{n=f[r/g]} \sqrt{(r^2 - (ng)^2)} \right) - 4r \right) h \quad (2.7)$$

where h is the height of specimen. The sum of the horizontal grain boundary surface areas is designated as

$$s_h = f \left[\frac{h}{g} - 1 \right] \pi r^2 \quad (2.8)$$

where $f [h/g-1]$ is the greatest integer function. The internal grain boundary surface area can be thus denoted as

$$s_{\text{internal}} = s_v + s_h = \left(8 \left(\sum_0^{n=f[r/g]} \sqrt{(r^2 - (ng)^2)} \right) - 4r \right) h + f \left[\frac{h}{g} - 1 \right] \pi r^2 \quad (2.9)$$

The total grain boundary surface area is

$$s_{\text{total}} = s_{\text{internal}} + 2\pi r^2 + 2r\pi h \quad (2.10)$$

The ratio of the internal grain boundary surface area to the total grain boundary surface area can be finally obtained in the following based on the above equations.

$$\frac{s_{\text{internal}}}{s_{\text{total}}} = \frac{s_{\text{internal}}}{s_{\text{internal}} + 2\pi r^2 + 2r\pi h} \quad (2.11)$$

Figure 2.6 shows the change of $s_{\text{internal}}/s_{\text{total}}$ with the grain and specimen sizes. From the figure, it can be seen that the $s_{\text{internal}}/s_{\text{total}}$ decreases with the increase of grain size and the decrease of specimen size. The change of $s_{\text{internal}}/s_{\text{total}}$ thus has a good correlation with size effect. The size effect on work-hardening behavior is studied based on $\sigma\theta-\sigma$ plot ($\theta = d\sigma/d\varepsilon$, which is called hardening coefficient), as shown in Fig. 2.7. The $\sigma\theta-\sigma$ plot actually presents three hardening stages of polycrystal [32]. Each stage is related to a specific plastic deformation mechanism. Stage I corresponds to the microplasticity where the hardening rate significantly decreases with the increase of flow stress and single slip occurs in most of the grains [33]. Stage II, which is called pure hardening stage, refers to the linear region in the $\sigma\theta-\sigma$ plot. In this hardening stage, multiple slip takes place, resulting in the formation of dislocation cells. The work-hardening effect is caused by the increase of dislocation density, leading to the entanglement of dislocation and prohibiting the dislocation motion. Stage III begins at the point where the downward curvature occurs. It is resulted from the negative contribution on strain hardening by dynamic recovery. The hardening rate in Stage III, which is sensitive

Fig. 2.6 Change of $s_{\text{internal}}/s_{\text{total}}$ with the grain and specimen sizes [21]

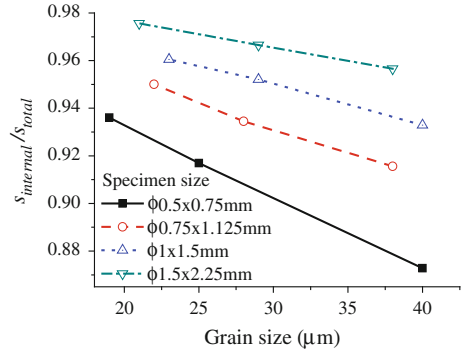
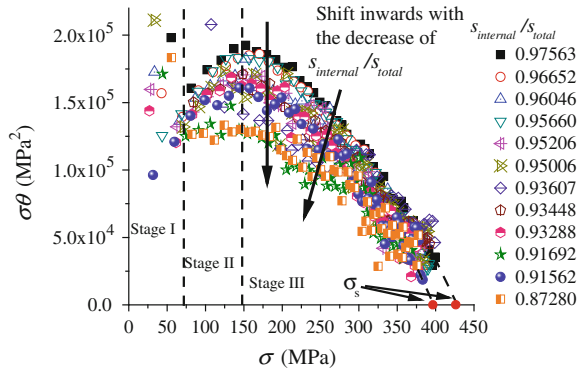


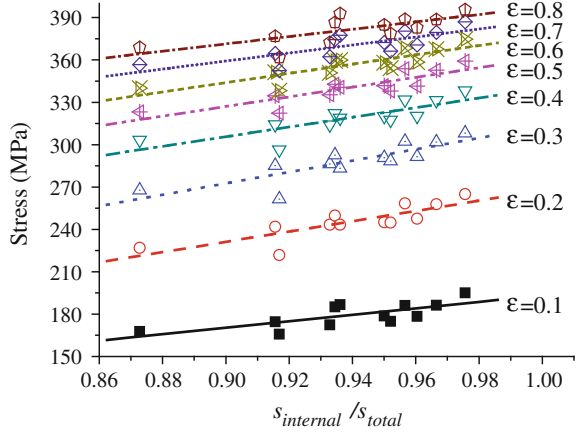
Fig. 2.7 The $\sigma\theta$ - σ plots with different values of $s_{\text{internal}}/s_{\text{total}}$ [21]



to forming temperature and stain rate, is characterized by the superposition of pure hardening process and the additional softening process [34]. The contribution from the pure hardening process to the hardening coefficient (θ) is almost constant. However, the influence of softening process increases with stress until the contributions from both processes balance the hardening completely at the saturation stress (σ_s) at which the material does not exhibit hardening behavior. The saturation stress is shown in the σ -axis of Fig. 2.7.

Based on the $\sigma\theta$ - σ plot shown in Fig. 2.7, it can be seen that the curve shifts inwards, and the slope of Stage II and the saturation stress decrease with $s_{\text{internal}}/s_{\text{total}}$. This reveals that the contribution from pure hardening process decreases. These phenomena could be attributed to the decrease of internal grain boundary fraction, which plays a significant role on material strengthening behavior. The material nature changes from polycrystal to single crystal with the decreasing $s_{\text{internal}}/s_{\text{total}}$. Figure 2.8 shows the change of flow stress with $s_{\text{internal}}/s_{\text{total}}$ and the flow stress has a linear relationship with $s_{\text{internal}}/s_{\text{total}}$ at a given strain. This further verifies that the size effect is caused by the change of internal grain boundary surface fraction.

Fig. 2.8 Change of the flow stress with $s_{\text{internal}}/s_{\text{total}}$ at a given strain [21]



2.2.4 Mixture Model

2.2.4.1 Iso-Strain-Based Model

Based on the assumption that there is an incompatibility zone with a few micrometers width at grain boundary, and the grain boundary and grain interior undergo the same deformation (iso-strain condition), Kocks [35] described the flow stress of materials in consideration of the flow stresses and volume fractions of grain boundary and interior with Voigt model [36] in the following:

$$\sigma = f_{gb}\sigma_{gb} + f_{gi}\sigma_{gi} \quad (2.12)$$

where f_{gb} and f_{gi} are the fractions of grain boundary and grain interior, respectively. σ_{gb} and σ_{gi} are their corresponding flow stresses. The Voigt model actually considers the materials of mixture aligning in the direction of the applied load, as shown in Fig. 2.9. Meyers and Ashworth [18] assumed that the form of grain is spherical with the diameter of d and the boundary thickness of λ . The fraction of grain boundary is

$$f_{gb} = \frac{\frac{1}{4}\pi[d^2 - (d - 2\lambda)^2]}{\frac{1}{4}\pi d^2} = 4\left[\frac{\lambda}{d} - \left(\frac{\lambda}{d}\right)^2\right], \quad (2.13)$$

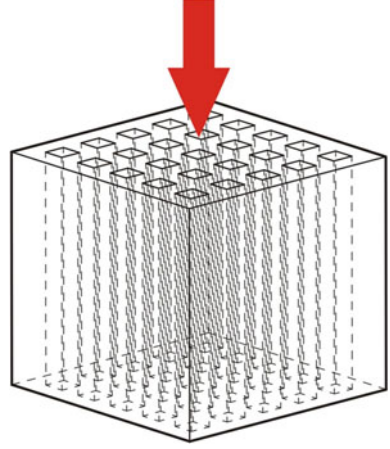
The fraction of grain interior is

$$f_{gi} = \frac{(d - 2\lambda)^2}{d^2} = 1 - f_{gb} \quad (2.14)$$

Substituting Eqs. (2.13) and (2.14) into Eq. (2.12) gives

$$\sigma = \sigma_{gi} + 4(\sigma_{gb} - \sigma_{gi})\lambda d^{-1} - 4(\sigma_{gb} - \sigma_{gi})\lambda^2 d^{-2} \quad (2.15)$$

Fig. 2.9 Schematic illustration of the iso-strain model [81]



Eq. (2.15) can be rewritten based on Hall–Petch relation

$$\sigma = \sigma_{gi} + \left[4(\sigma_{gb} - \sigma_{gi})\lambda d^{-1/2} - 4(\sigma_{gb} - \sigma_{gi})\lambda^2 d^{-3/2} \right] d^{-1/2} \quad (2.16)$$

Comparing Eq. (2.16) with Eq. (2.1) gives

$$\begin{aligned} K_{hp} &= 4(\sigma_{gb} - \sigma_{gi})\lambda d^{-1/2} - 4(\sigma_{gb} - \sigma_{gi})\lambda^2 d^{-3/2} \\ &= 4(\sigma_{gb} - \sigma_{gi})\lambda \left(d^{-1/2} - \lambda d^{-3/2} \right) \end{aligned} \quad (2.17)$$

Since the Hall–Petch constant, K_{hp} , is independence of grain size (d). It thus suggests

$$\lambda \left(d^{-1/2} - \lambda d^{-3/2} \right) = C \quad (2.18)$$

where C is a constant. Another mixture model based on the assumption of grain with cubical form was proposed by Hirth [31] in the following:

$$\sigma = \sigma_{gi} + (\sigma_{gb} - \sigma_{gi})(4d\lambda - 4\lambda^2)d^{-2} \quad (2.19)$$

The expression based on the Hall–Petch relation can be obtained by rewriting Eq. (2.19) as follows:

$$\sigma = \sigma_{gi} + \left[(\sigma_{gb} - \sigma_{gi})(4d\lambda - 4\lambda^2)d^{-3/2} \right] d^{-1/2} \quad (2.20)$$

It can be seen that Eq. (2.20) gives the expression of K_{hp} which is the same as that in Eq. (2.17). It therefore suggests that the assumptions of the spherical and cubical grain forms are equivalent. As shown in Fig. 2.10, there are different fractions of grain boundary and interior at different sections. The mean grain diameter (\bar{d}) and grain boundary thickness ($\bar{\lambda}$) are used and given by [18, 37, 38]

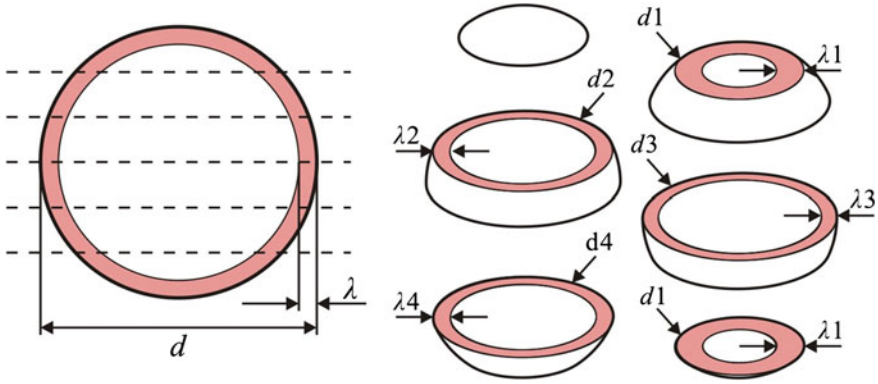


Fig. 2.10 Schematic illustration of different grain diameters and the thicknesses at different sections [81]

$$\bar{d} = \frac{\pi}{4}d, \quad \bar{\lambda} = 1.57\lambda \quad (2.21)$$

Substituting Eq. (2.21) into Eq. (2.15) gives

$$\sigma = \sigma_{gi} + 8(\sigma_{gb} - \sigma_{gi})\lambda d^{-1} - 16(\sigma_{gb} - \sigma_{gi})\lambda^2 d^{-2} \quad (2.22)$$

Meyers and his colleagues proposed the following [37, 38]:

$$K_{hp} = 8K_{MA}(\sigma_{gb} - \sigma_{gi}) \quad (2.23)$$

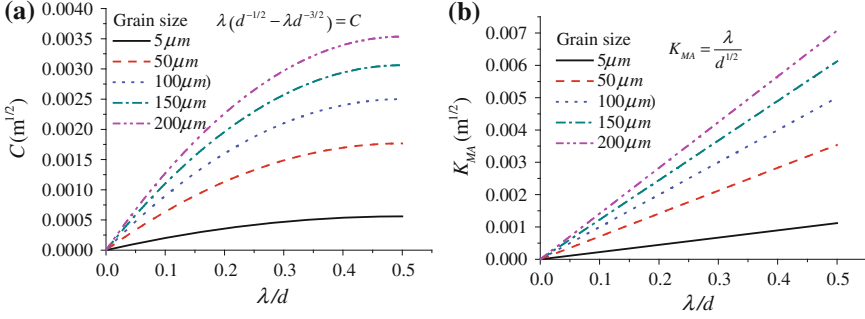
where

$$K_{MA} = \frac{\lambda}{d^{1/2}} \quad (2.24)$$

Based on the above equations, the most critical issue is to define the mechanical properties of grain boundary and interior. If there is about one grain over the specimen thickness, the grain boundary strengthening effect is assumed not significant. It can thus be used to model the mechanical properties of grain interior. The atoms in grain boundary are more reactive as they are more disordered compared with the atoms at grain interior. Prior studies have shown that the atomic structure at grain boundary is similar to amorphous structure [39–41]. Numerous studies assume that the mechanical properties of grain boundary are like the ones of amorphous materials. Based on this assumption, Kim [42] and Carsley et al. [43] conducted the investigation of grain size effect on the hardness of materials. Zhou et al. [44] modeled the grain size effect on the elastic modulus and stress–strain relation. Drucker’s constitutive equation [45] has been proven to be suitable for modeling of the plastic behavior of amorphous materials [46] and it was thus employed to describe the plastic behavior of amorphous grain boundary phase in prior studies [44, 47, 48]. The Drucker’s constitutive equation is given by

Table 2.1 The material parameters of grain boundary of pure copper [44]

E (GPa)	ν	n	σ_y^{gb} (MPa)	m	h (MPa)
75.9	0.35	0.4	426.28	0.4	426.28

**Fig. 2.11** Change of **a** C and **b** K_{MA} with grain boundary fraction [81]

$$\sigma_y^{gb} = \sigma_y^{gb} + mp + h(\varepsilon^{gb})^n \quad (2.25)$$

where σ_y^{gb} , m , h and n are the material constants of the grain boundary phase. $p = -\sigma_{kk}/3$ is the hydrostatic pressure. The material parameters in Eq. (2.25) for amorphous grain boundary phase of pure copper can be obtained from literature [44] and are presented in Table 2.1.

Equations (2.15)–(2.18) and Eqs. (2.22)–(2.24) are developed based on the different definitions of grain diameter and boundary thickness. The former is based on the section across the diameter of spherical grain, while the later is based on the averaged grain diameter and boundary thickness in consideration of the different sections of spherical grain. These models are examined in the following. The ratio of grain boundary thickness (λ) to grain diameter (d) is used to quantify the fraction of grain boundary. The changes of material constants, C and K_{MA} (in Eqs. (2.18) and (2.24)), with λ/d at a given grain size are shown in Fig. 2.11. Both of the constants increase with λ/d and grain size. Based on the known $K_{hp} = 0.11 \text{ MPa m}^{1/2}$, $\sigma_{gi} = 25 \text{ MPa}$, and the yield stress of grain boundary ($\sigma_{gb} = 426.28 \text{ MPa}$) of pure copper [37, 44], the material constants, C and K_{MA} for pure copper can be further estimated by Eqs. (2.17) and (2.23). They are $6.85 \times 10^{-5} \text{ m}^{1/2}$ and $3.43 \times 10^{-5} \text{ m}^{1/2}$, respectively. Therefore, the change of grain boundary fraction and its thickness can be determined, as shown in Fig. 2.12. It can be seen that the estimated values based on K_{MA} is lower than the one based on C . Both results, however, present the same tendency that the grain boundary thickness decreases and its volume fraction increases with the decrease of grain size. The variation of grain boundary thickness is not proportional to the variation of grain size. Based on the measured flow stresses by experiment and Eq. (2.25), the change of the fraction of grain boundary with strain and N can be identified

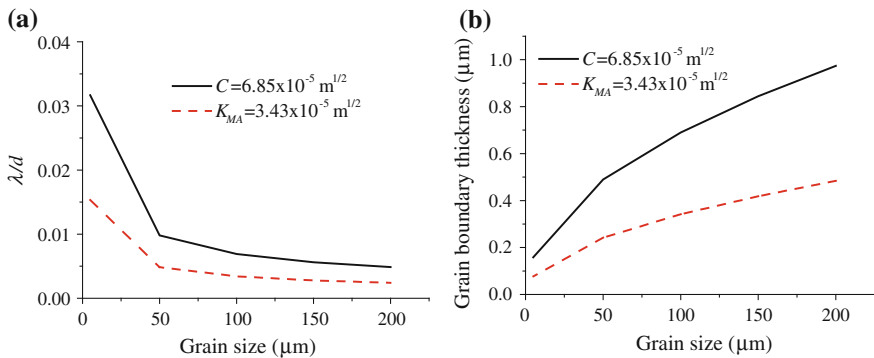


Fig. 2.12 Change of **a** grain boundary fraction and **b** thickness with the grain size of pure copper [81]

with Eqs. (2.15) and (2.22) by using the numerical method, as shown in Figs. 2.13 and 2.14, respectively. The fraction of grain boundary increases with strain and N . The estimated grain boundary fraction by Eq. (2.15) is about two times higher than that by Eq. (2.22).

2.2.4.2 Mixed Iso-Strain and Iso-Stress-Based Model

In the case that the grain boundary and grain interior are assumed to have the same stress (iso-stress condition), the flow stress of material can be represented based on Reuss model [49] as follows:

$$\frac{1}{\sigma} = \frac{f_{gb}}{\sigma_{gb}} + \frac{(1 - f_{gb})}{\sigma_{gi}} \quad (2.26)$$

The iso-stress-based model considers the materials of the mixture aligning perpendicular to the direction of the applied load, as shown in Fig. 2.15. Most of the mechanical behaviors of material fall in between the iso-stress and iso-strain models [44]. The iso-strain-based model is thus considered as an upper bound model, while the iso-stress-based model as a lower bound model. The material is assumed to be composed of an array of repeating cubic unit grain, as shown in Fig. 2.16. The unit grain has two phases, viz., grain boundary and interior. The contribution of flow stress from the side boundary is described based on the iso-strain model, while contributions from the top and bottom boundaries are represented by the iso-stress model. The combined flow stress of the grain interior and the side boundary is calculated by

$$\sigma_{gi+gb,s} = \sigma_{gi} \frac{f_{gi}}{f_{gi} + f_{gb,s}} + \sigma_{gb} \frac{f_{gb,s}}{f_{gi} + f_{gb,s}} \quad (2.27)$$

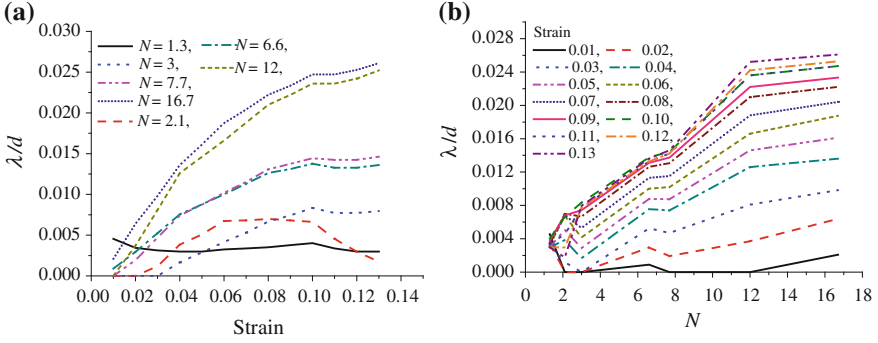


Fig. 2.13 Change of λ/d with **a** strain and **b** N (Based on Eq. (2.15)) [81]

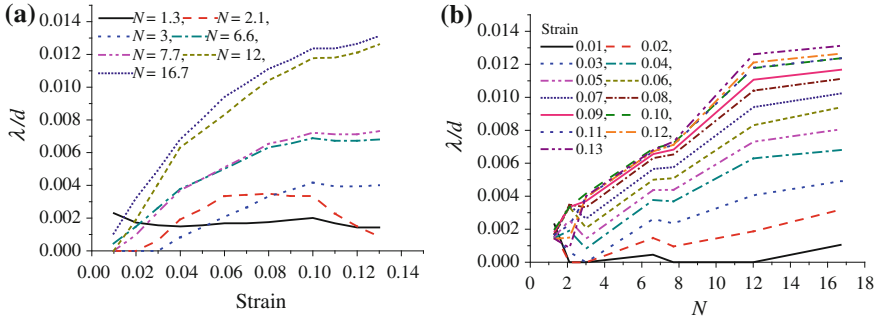


Fig. 2.14 Change of λ/d with **a** strain and **b** N (Based on Eq. (2.22)) [81]

The combined flow stress of the unit grain is

$$\sigma = \left(\frac{f_{gi} + f_{gb,s}}{\sigma_{gi+gb,s}} + \frac{f_{gb,tb}}{\sigma_{gb}} \right)^{-1} \quad (2.28)$$

where $f_{gb,tb}$ is the volume fraction of the top and bottom boundary, while $f_{gb,s}$ is the volume fraction of the side boundary, as shown in Fig. 2.16. The volume fraction of each component can be calculated from the geometric point of view in the following:

$$f_{gi} = \frac{(d - 2\lambda)^3}{d^3} \quad (2.29)$$

$$f_{gb,s} = \frac{d^3 - (d - 2\lambda)^3 - 2d^2\lambda}{d^3} = 1 - \frac{(d - 2\lambda)^3}{d^3} - \frac{2\lambda}{d} \quad (2.30)$$

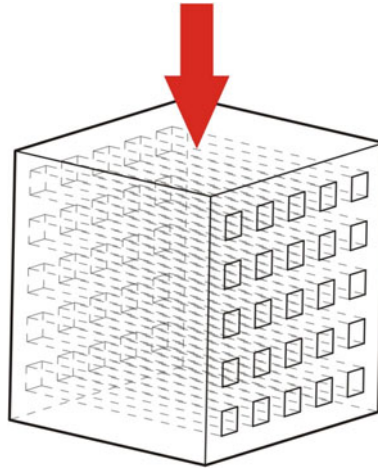


Fig. 2.15 Schematic illustration of the iso-stress model [81]

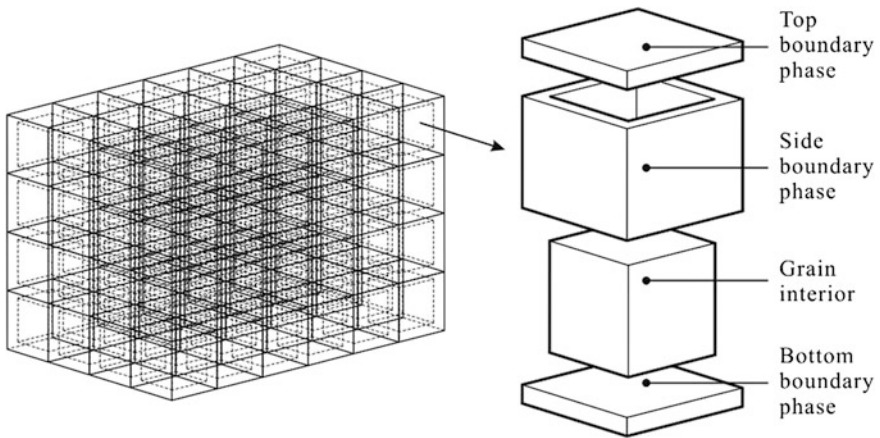


Fig. 2.16 Structure of the unit grain [81]

$$f_{gb,tb} = \frac{2d^2\lambda}{d^3} = \frac{2\lambda}{d} \tag{2.31}$$

where d is the grain size and λ is the thickness of grain boundary. Based on Eqs. (2.27)–(2.31) and the properties of grain interior and boundary defined in the previous section, the variation of grain boundary fraction can be determined by using the numerical method, as shown in Fig. 2.17. The results show the tendency, that the grain boundary fraction increases with strain and N , is the same as the one obtained in the previous section. The estimated grain boundary fraction falls in between the results (Figs. 2.13 and 2.14) predicted by the previous two models.

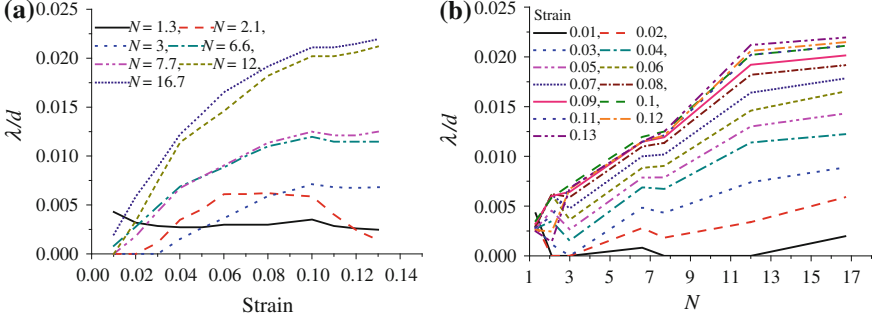


Fig. 2.17 Change of λ/d with **a** strain and **b** N (Based on Eq. (2.28)) [81]

2.2.4.3 Finite Element Simulation

Based on Figs. 2.13, 2.14, and 2.17, it can be seen that Eqs. (2.15), (2.22), and (2.28) have different estimations on grain boundary fraction. Finite element (FE) simulation, which provides an advanced analysis of material deformation behavior, is thus employed to evaluate the accuracy of different models. The number of grains at each section of the material is assumed to be almost the same, as illustrated in Fig. 2.18. Therefore, it can be considered as the plane strain deformation condition. The model is further simplified to be a single grain with the side length of d and the boundary thickness of λ . The simulations are conducted in a commercial CAE system, ABAQUS. The forming material is modeled as an elastic-plastic body and meshed with four-node bilinear quadrilateral elements. Figure 2.19 shows the simulation results of the change of flow stress with N for a given strain. Although the estimated grain boundary thicknesses are different by using different models, the FE simulation results based on those estimated grain thicknesses generally have a satisfactory agreement with the experimental results. By using the thickness estimated by Eq. (2.15), it yields the highest flow stress among three models and then followed by the results based on Eqs. (2.28) and (2.22). It is difficult to evaluate which model is relatively accurate, the averaged error is thus used to quantify the accuracy of each model and expressed as:

$$e = \frac{\int \left(\frac{\int \left| \frac{(\sigma_e - \sigma_m)}{\sigma_e} \right| \times 100\% | dN}{\int dN} \right) d\varepsilon}{\int d\varepsilon} \quad (2.32)$$

where σ_e and σ_m are the flow stresses obtained from experiment and the models for a given strain, respectively. The estimation errors are 4.0, 3.8, and 3.5 % for Eqs. (2.15), (2.22), and (2.28), respectively. Therefore, Eq. (2.28), which is the mixed iso-strain and iso-stress-based model, performs a little bit better than the others.

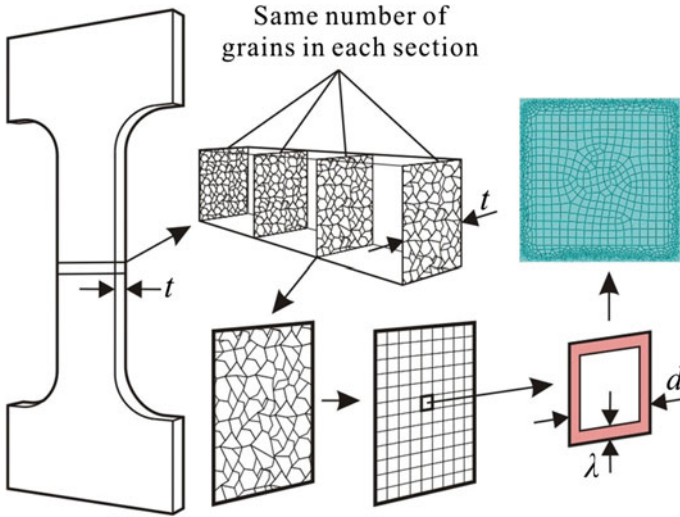


Fig. 2.18 Model simplification [81]

2.2.5 Surface Layer Model

Miyazaki et al. [27] found that the dislocation tangles only occur near the threefold node of grain boundaries and a few dislocations are heterogeneously distributed inside the grain at the surface layer of material. It is suggested that the deformation behavior of the surface material is different from the inside one. Surface grains have less constraint compared with internal grains. The dislocation structure in surface grains is thus different from that of internal grains [22, 27] and the surface grains have lower flow stress [50, 51]. The decrease of flow stress could be attributed to the change of the volume fraction of surface grains. The flow stress can thus be determined by both the surface and internal grains [52–55] and expressed as:

$$\sigma(\varepsilon) = \alpha_s \sigma_s(\varepsilon) + \alpha_i \sigma_i(\varepsilon) \quad (2.33)$$

where $\sigma_s(\varepsilon)$ and $\sigma_i(\varepsilon)$ are the flow stresses of surface and internal grains, respectively. They are the function of strain. α_s and α_i are the volume fractions of surface and internal grains. The number of grains in the cross-section of workpiece is large and the volume fraction of surface grains is small when the workpiece size is in macroscale and the grain size is fine. When the workpiece size is decreased to microscale and the grain size is large, there are only a few grains constituting the workpiece and the volume fraction of surface grains increases tremendously as shown in Fig. 2.20, which results in the decrease of flow stress.

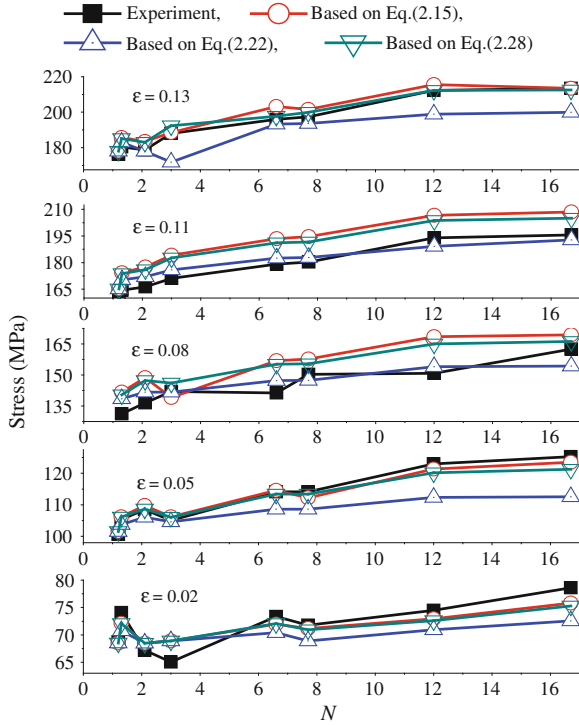


Fig. 2.19 Validation of the material models [81]

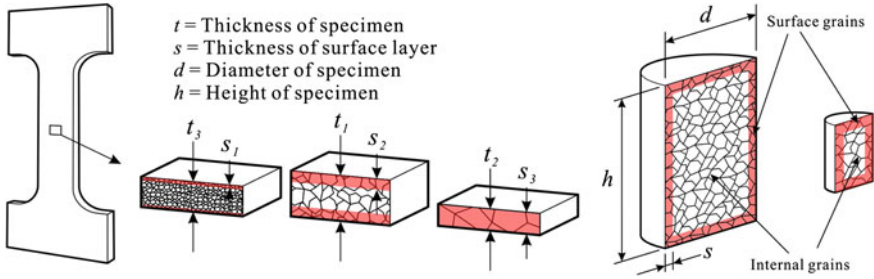


Fig. 2.20 Change of the volume fraction of surface grains with the change of specimen and grain sizes [16, 81]

2.3 Deformation Behavior

The specimen and grain sizes affect the material flow behavior in microforming processes. Figure 2.21 shows the end surfaces of the original and compressed Al6061 cylinders with different sizes. It can be seen that the shapes of the

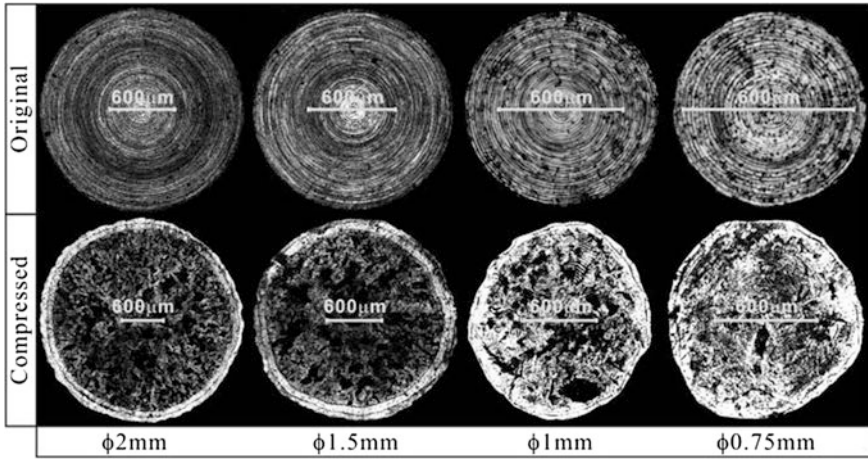
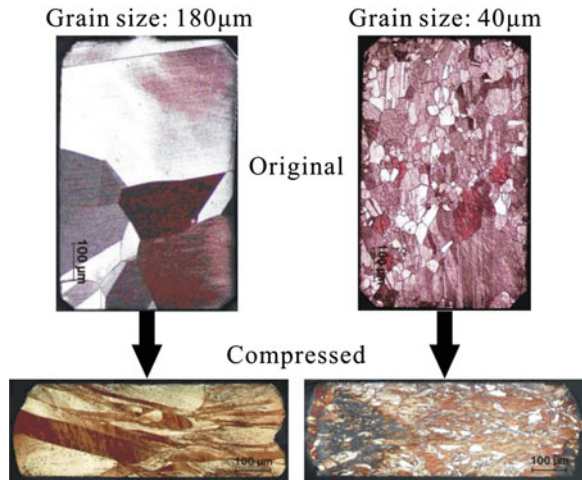


Fig. 2.21 End surfaces of the original and compressed Al6061 cylinders [16]

Fig. 2.22 Microstructures of the original and compressed copper cylinders with different grain sizes [82]



compressed specimens change from circular to irregular shape with the decrease of specimen size. A similar phenomenon is also observed in the compression of copper cylinders with the change of grain size, as shown in Fig. 2.22. Inhomogeneous deformation arises in the case with coarse grains.

2.3.1 Anisotropic Properties of Single Grain

The size effect on material flow behavior is related to the interaction among grains to maintain strain continuity across grain boundary. Grain deforms via slipping. The slip plane together with the slip direction constitutes the slip system. The slip

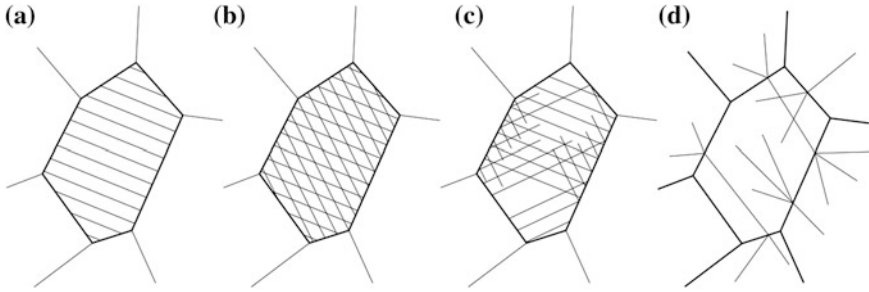
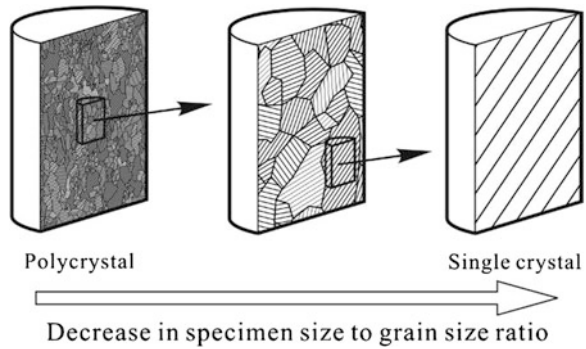


Fig. 2.23 Slip systems in different models, **a** Sachs model, **b** Taylor model, **c** Kocks and Canova model and **d** Leffers model

plane is the plane that has the greatest atomic density, while the slip direction is the closest-packed direction in the slip plane. Grain has a number of slip systems for deformation. Schmid and Boas [56] found that single crystal deforms when a critical shear stress is reached in a slip system. This criterion is applied by Sachs [57] who assumed that all the grains are deformed by single slip, as shown in Fig. 2.23a. However, this hypothesis neglects the strain compatibility at grain boundary. Taylor [58] assumed that each grain undergoes the same homogeneous strain, equal to the macroscopic strain. He suggested that all the grains are deformed homogeneously as long as at least five independent slip systems are activated, as shown in Fig. 2.23b. He further predicted the grain orientation factor (M), which relates macroscopic tension stress (σ) and shear stress (τ), has a value of 3.06 for random FCC polycrystal, which is in contrast to the value of 2.24 predicted by Sachs [57]. A modification of Taylor theory was then done by Kocks and Canova [59]. They proposed that the strain continuity can be maintained with less than five slip systems. Different slips may not be necessary to pass through the whole grain, as shown in Fig. 2.23c. Leffers [60] modified the Sachs model and proposed that the slip planes meet the grain boundary and the generated stress is relaxed by the second slip in the neighbor grains, as shown in Fig. 2.23d.

The irregular shape of the compressed specimen is caused by the random characteristics of grain size, form, and orientation. The deformation properties of a single grain are anisotropic. Since the polycrystalline material is composed of a large number of grains, the grains with different properties can be randomly and evenly distributed, resulting in the isotropic deformation behavior. When the size of workpiece is in microscale and the grain size is coarse, there is only a few grains in the workpiece and the even distribution of different grains no longer exists. The anisotropic properties of each grain become significant to the deformation behavior and lead to the inhomogeneous deformation. The deformation behavior of material in microforming could fall in between that of polycrystal and single crystal, as shown in Fig. 2.24. To minimize such kind of size effect, Eichenhueller et al. [61, 62] conducted the microforming at an elevated temperature, which is

Fig. 2.24 The transition of polycrystal to single crystal [16]



above room temperature and below recrystallization temperature. Their experimental results show that the homogeneous deformation can be achieved in extrusion process due to the dislocation movement thermally activated at the elevated temperature. It makes the unfavorably oriented grains plasticized and the strain incompatibility among grains decreased.

2.3.2 Modeling of Deformation Behavior

In compression and tensile tests, it can be found that the scatter effect of the obtained flow stress curves increases with the decreasing number of grains in testing materials. Figure 2.25 shows the obtained flow stress curves in the compression test of micro-cylinders with the dimension of $\text{Ø}0.5 \times 0.75$ mm and the grain size of 40 and 180 μm corresponding to the results shown in Fig. 2.22. The scatter effect of flow stress curve is caused by the grains with different sizes, shapes, and orientations unevenly distributed in the testing samples. Therefore, different flow stress curves should be used to model the deformation behaviors of testing materials with different grains. The flow stress of the testing material could be modeled with a composite model in the following:

$$\sigma(\varepsilon) = \sum_{i=1}^n V_i \cdot \sigma_i(\varepsilon) \quad (2.34)$$

where n is the total number of grains in the specimen. V_i is the volume fraction, or area fraction in two-dimensional case, of the i th grain. $\sigma_i(\varepsilon)$ is the flow stress of the i th grain and a function of strain considering work-hardening. Figure 2.26 shows a schematic illustration of a set of flow curves of specimens with the same geometry dimension and mean grain size. The scatter effect of the flow stress curve could be modeled with a normal distribution function, which is one of the most commonly observed random variables with a bell-shaped probability distribution.

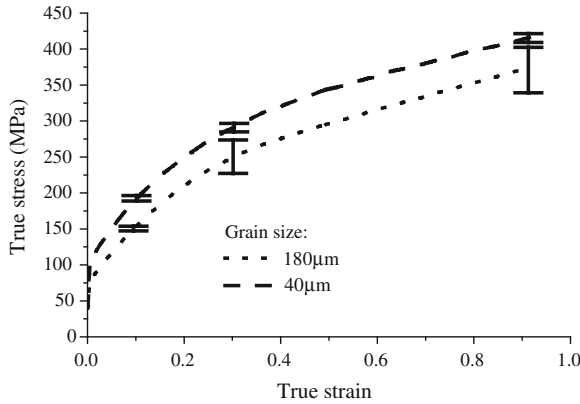


Fig. 2.25 Flow stress curves of micro-cylinders with the dimension of $\emptyset 0.5 \times 0.75$ mm and the grain size of 40 and 180 μm [82]

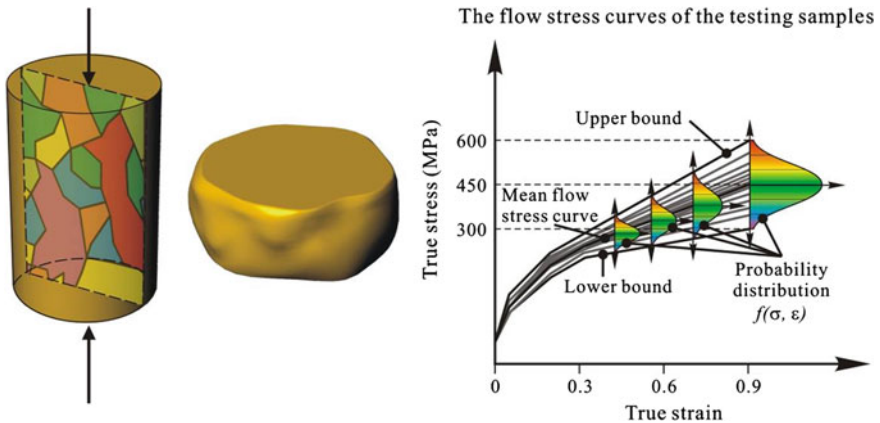


Fig. 2.26 Schematic illustration of the modeling of scatter effect with a normal distribution function [82]

Taking the case with only four grains in the sample and each grain having the same volume in the material as an instance, the deformation behavior of each grain is described with its corresponding flow stress curve and the averaged flow stress curve could be used to describe the deformation behavior of the entire sample material based on the composite model. To generate the upper bound of the measured flow stress curves for the testing samples, the flow stress curves of some grains must be higher than the upper bound of the measured flow stress curves of the testing samples, as shown in Fig. 2.27a. Similarly, the flow stress curves of some grains must be lower than the lower bound of the measured flow stress curves, as shown in Fig. 2.27b. Therefore, the degree of spread of the grain properties must be wider than that of the testing sample properties, as shown in Fig. 2.27c, while the mean flow stress curve of the grains is the same as the

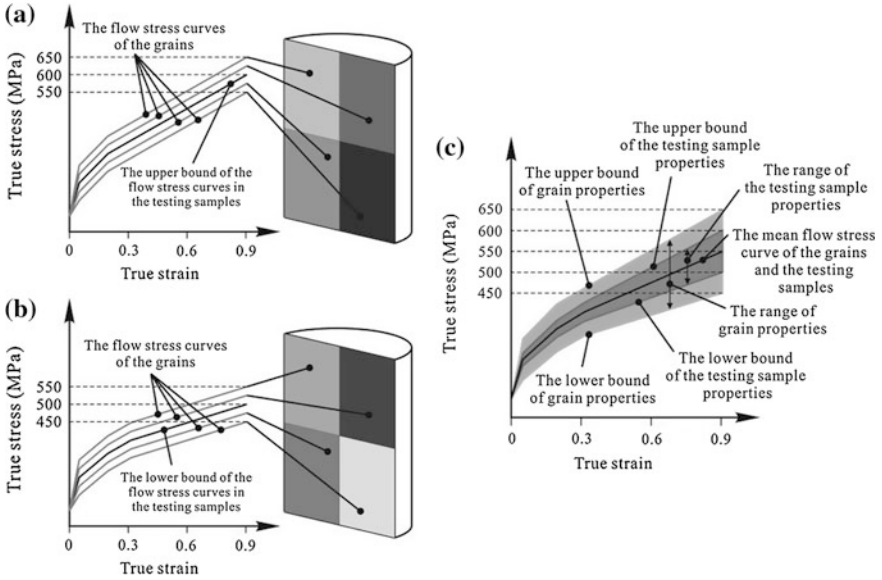


Fig. 2.27 Upper and lower bounds of the flow stresses of grain and the testing sample [82]

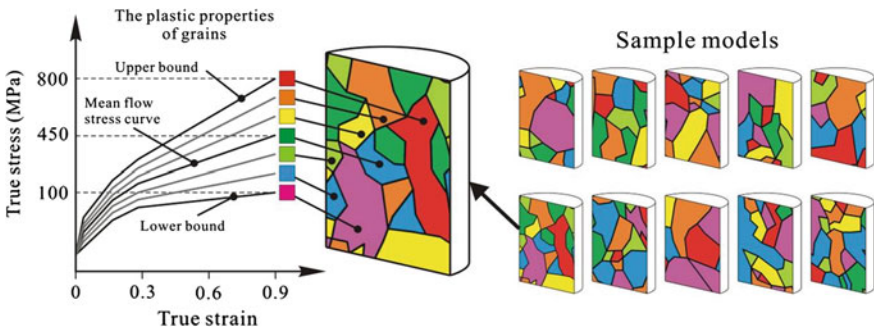


Fig. 2.28 Random assignment of grain properties on the metallographies of the sample models [82]

measured mean flow stress curve of the testing samples. This assumption could also be adopted in the case shown in Fig. 2.26 and the schematic illustration of the grain properties is shown in Fig. 2.28. In Fig. 2.28, the grain properties are divided into several groups represented by their corresponding flow stress curves, which are evenly spaced within the upper and lower bounds. When the metallographies of the testing samples are known, the volume/area fraction of each grain in the testing sample can be estimated. The properties can then be assigned to the grains on the metallographies randomly. The flow stress curves of the testing samples and the scatter effect can be estimated based on Eq. (2.34).

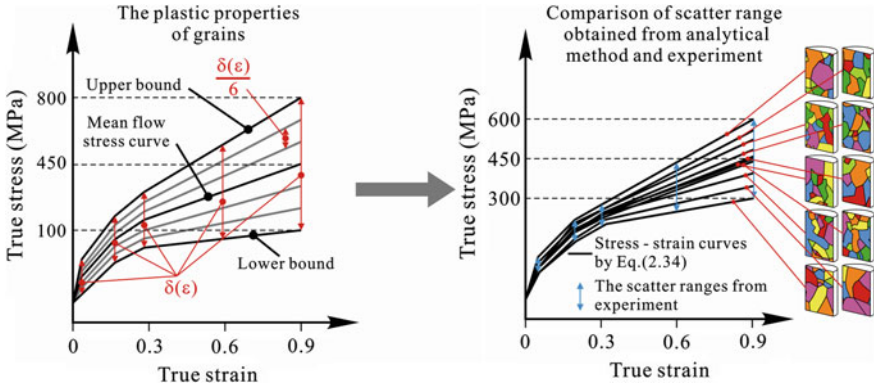


Fig. 2.29 Evaluation of the degree of spread $\delta(\epsilon)$ of the flow stress curves of grains [82]

As shown in Fig. 2.29, the properties of grains are determined via evaluating the degree of spread $\delta(\epsilon)$ of the flow stress curves of grains, estimating the scatter effect of the testing samples with Eq. (2.34), and matching the estimated scatter effect with the physical experimental results. In addition, Fig. 2.30 shows a schematic illustration of the grain size effect on material flow stress. The size effect on inhomogeneous deformation behavior and the scatter of flow stress can be modeled with the degree of spread $\delta(\epsilon)$ in the flow stress curves of grains, while the size effect on the decrease of flow stress can be modeled with the mean flow stress $\sigma_m(\epsilon)$ of grains. The larger ratio of specimen size to grain size (D/d), the stronger grain boundary hardening effect, and further the higher mean flow stress of grains. In addition, the wider spread of the flow stress curves of grains, the greater scatter effect of the obtained data, and the higher degree of inhomogeneous deformation.

2.3.2.1 Simulation of Micro-Compression

Based on the results of compression test as shown in Fig. 2.25, the modeling methodology presented in the previous section is demonstrated. First, the metallography of the annealed pure copper is extracted from physical sample, as shown in Fig. 2.31. Different groups of the grain plastic properties are evenly and randomly distributed in the metallography presented in Fig. 2.32. Twenty regions with an approximate D/d ratio of 2.8 are extracted as the sample models for estimation of the upper and lower bounds of grain flow stress curves. The ratio is the same as that of the physical samples with the dimension of $\text{Ø}0.5 \times 0.75$ mm and the grain size of $180 \mu\text{m}$. The area fraction of each grain in each sample model could be obtained using computer-aided design (CAD) system. Based on the aforementioned explanation, the degree of spread of the grain flow stress curves must be larger than that of the testing samples. Therefore, the scatter range of the

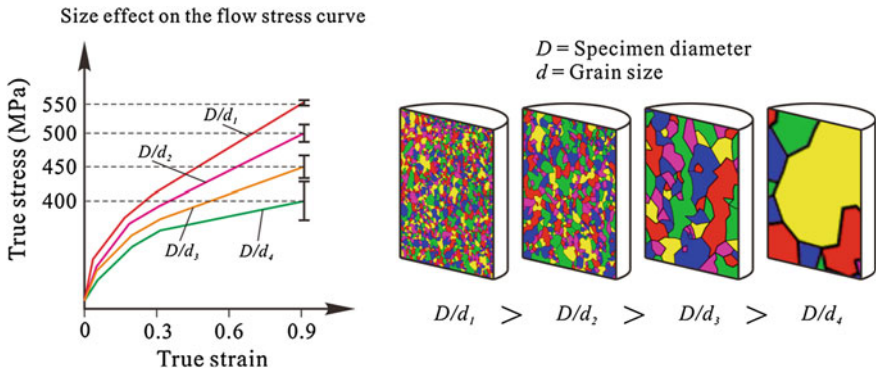


Fig. 2.30 Schematic illustration of grain size effect [82]

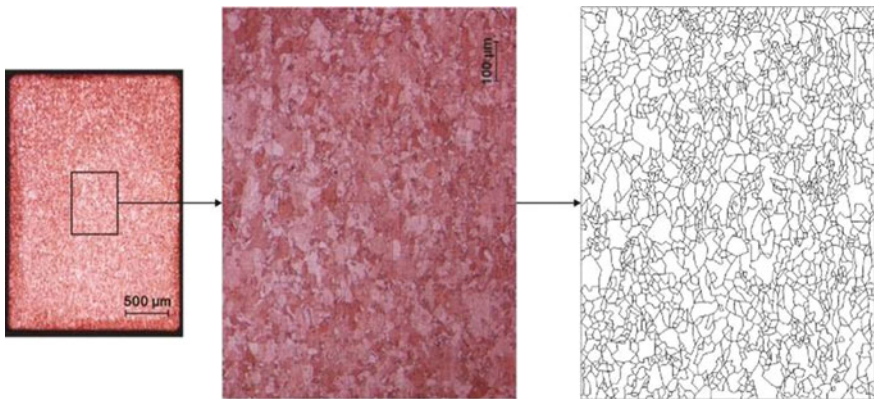


Fig. 2.31 Metallography of the annealed pure copper [82]

flow stress curves (shown in Fig. 2.25) of the samples with the geometry dimension of $\text{Ø}0.5 \times 0.75 \text{ mm}$ and the grain size of $180 \mu\text{m}$ could be considered as a basis to estimate the upper and lower bounds of the grain flow stress curves. The grain properties can be identified by evaluating the degree of spread $\delta(\epsilon)$ of grain flow stress curves, and estimating the flow stress curves of sample models and the scatter range using Eq. (2.34). The identified grain properties and the corresponding 20 estimated flow stress curves from the sample models are shown in Fig. 2.33. The identified flow stress curves of grains are used for 2D axisymmetric and 3D simulations using the commercial computer-aided engineering (CAE) system, ABAQUS.

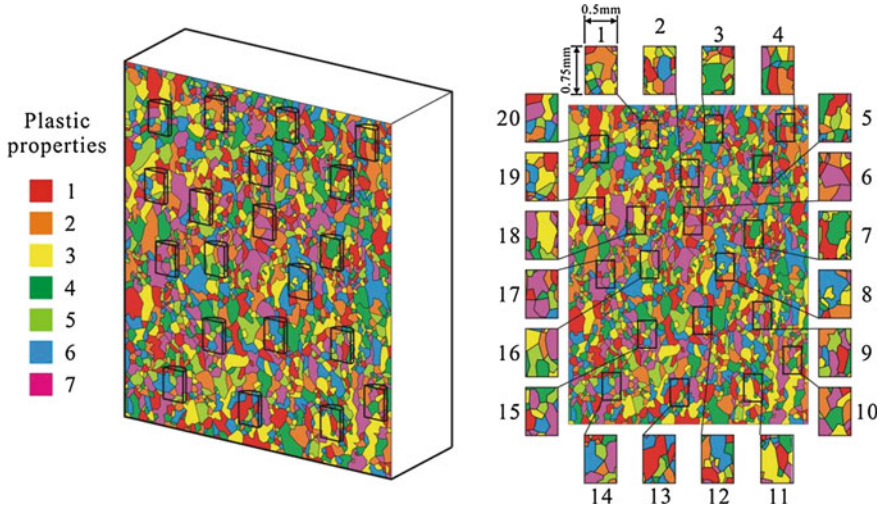


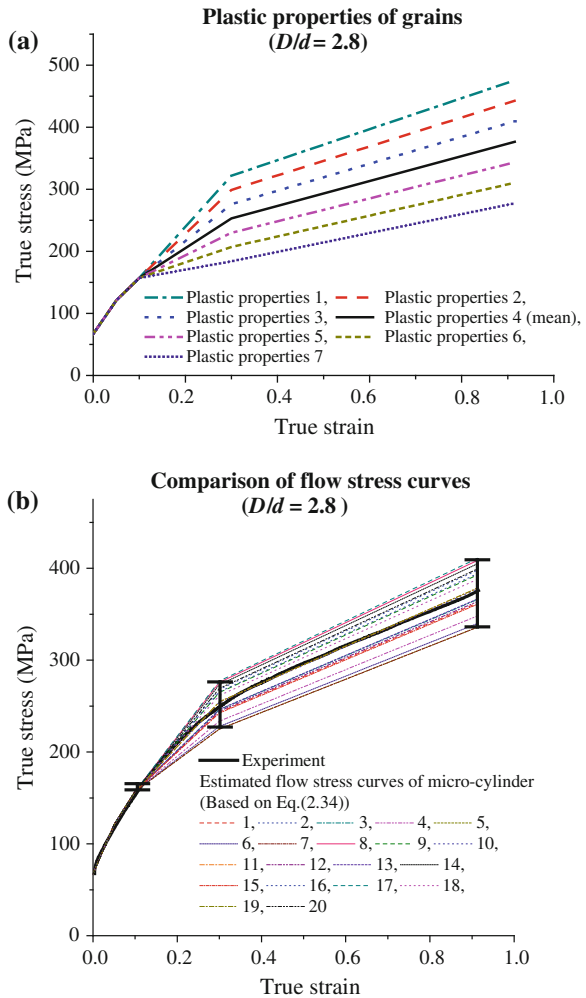
Fig. 2.32 The selected 20 cases for estimation of the grain properties in the sample with the D/d ratio of 2.8 [82]

2.3.2.2 2D Axisymmetric Model

To simulate the grain size effect on the material deformation behavior, the grain interior and grain boundary are considered as a single body, while the change of grain boundary strengthening effect due to the change of D/d ratio is taken into account with varying the mean flow stress of grains based on the modeling methodology presented in Sect. 2.3.2. By using the 2D axisymmetric model to simulate the deformation behavior of specimen with the D/d ratio of 2.8, four half of the section of each selected region shown in Fig. 2.32 is simulated with four-node bilinear axisymmetric quadrilateral element. Punch and counter punch are set to be rigid bodies, while the specimen is defined as an elastic–plastic body. The identified properties shown in Fig. 2.33a are assigned to the grain models and the friction coefficient is set to be 0.1. The shapes of the side profiles of the simulated cases, as shown in Fig. 2.34, are irregular and the deformation is inhomogeneous, which has a good agreement with the experimental results shown in Fig. 2.22. Furthermore, the simulated flow stress curves are shown in Fig. 2.35. It can be seen that some simulated flow stress curves are out of the range of the experimental results.

To simulate the deformation behavior of the specimen with the D/d ratio of 12.5 (the case with the dimension of $\text{Ø}0.5 \times 0.75$ mm and the grain size of $40 \mu\text{m}$), it needs to consider the fact that the grain boundary hardening effect is higher than that of the case with the D/d ratio of 2.8. Based on the grain properties in the case with the D/d ratio of 2.8 (Fig. 2.33a), the mean flow stress of the grains is increased to the mean flow stress curve of the testing specimens with the grain size of $40 \mu\text{m}$ (Fig. 2.25), while the parameter $\delta(\varepsilon)$ keeps the same. The material

Fig. 2.33 The estimated grain properties in the case with the D/d ratio of 2.8 [82].
a The identified plastic properties of grains [82].
b The comparison of flow stress curves [82]



properties of the grains in the specimen with the D/d ratio of 12.5 are shown in Fig. 2.36. Figure 2.37 shows the 20 selected sections of the axisymmetric sample models with an approximate D/d ratio of 12.5. Figure 2.38 shows the four simulated models results. The simulated result shows that the specimens perform a higher degree of homogeneous deformation when compared with the case with the D/d ratio of 2.8 based on the shape of side profiles (Fig. 2.34). The simulated flow stress curves are shown in Fig. 2.39. It can be seen that the simulated scatter effect is still larger than the experimental result, but the error is less than that in the case with the D/d ratio of 2.8 (Fig. 2.35). The error is due to the fact that the axisymmetric model only considers half of the section and some grain properties with higher or lower flow stress may dominate in the model, resulting in the higher or

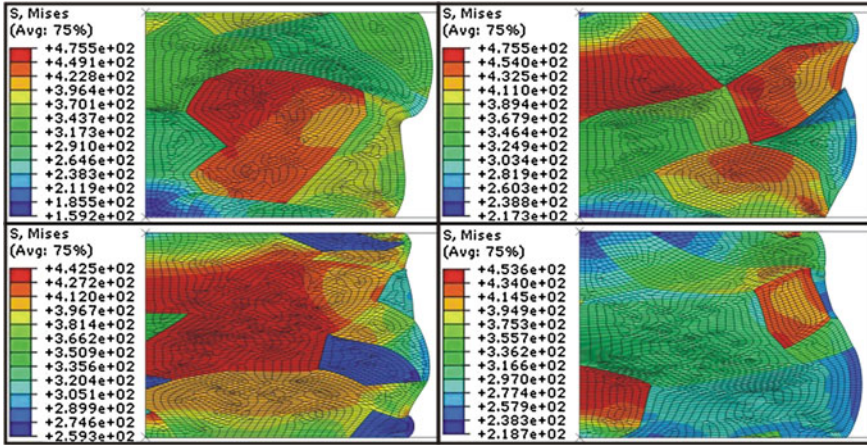
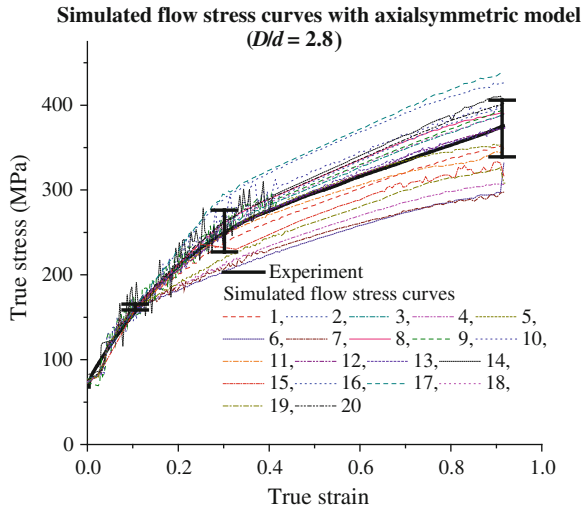


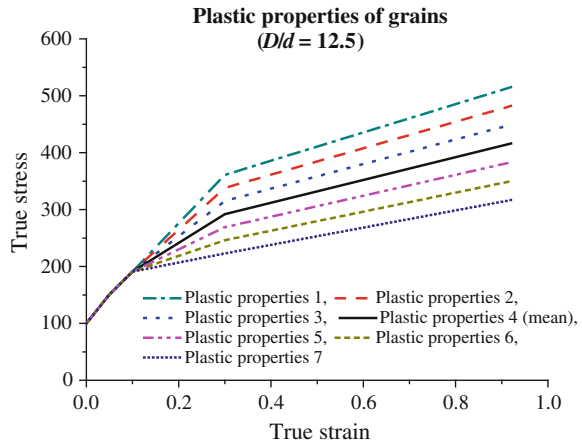
Fig. 2.34 The simulated stress distributions in the 2D axisymmetric models with the D/d ratio of 2.8 [82]

Fig. 2.35 The simulated flow stress curves in the axisymmetric model with the D/d ratio of 2.8 [82]



lower mean flow stress in simulation. The error of the simulated result can be addressed with Fig. 2.40, which represents a metallography of sample model. The grid represents a unit area and the thick line stands for the grain boundary. Different colors and numbers in the grids are used to differentiate the properties of grains. The larger the value, the higher the flow stress. In the axisymmetric model where only half of the section is considered, the area fraction with the high value of 7 dominates on the left half and the area fraction with the low value of 1 dominates on the right half. The mean values of the left half (5) and the right half (2.3) thus become higher and lower than the mean value of the whole section (3.7),

Fig. 2.36 The flow stress curves of the grains in the case with the D/d ratio of 12.5 [82]



respectively. This error decreases with the increase of D/d ratio since the individual grain properties become insignificant to the properties of the whole material model.

2.3.2.3 3D Full-Scale Model

In order to have an in-depth investigation on modeling of the deformation behavior in micro-compression, 3D full-scale simulation is conducted with eight-node linear brick element. Grain is represented as a cube for simplification. Figure 2.41 illustrates a 3D metallography assembled with cubic grains and the grain properties are randomly assigned. Figure 2.41 illustrates a 3D metallography assembled with cubic grains and the grain properties are randomly assigned. The identified grain properties shown in Figs. 2.33a and 2.36 are employed in the full-scale models for simulating the deformation behaviors of the specimens with the D/d ratio of 2.8 and 12.5, respectively. The FE model with the D/d ratio of 12.5 is shown in Fig. 2.42. Twenty sample models are simulated in both the cases with the D/d ratio of 2.8 and 12.5, respectively. Four simulation results of the deformed specimens in both the cases are shown in Figs. 2.43 and 2.44, respectively. Based on the simulated contours of side surfaces of the sample models, it can be seen that the size effect on the increasing degree of inhomogeneous deformation with the decrease of D/d ratio can be simulated. The simulated flow stress curves in both the cases are shown in Figs. 2.45 and 2.46, respectively. The results show that the scatter effect of the flow stress curve increases with the grain size and the simulated scatter range has a good agreement with the experimental result. Based on the above simulated results, it is concluded that the simulation of grain size effect in micro-compression is feasible with the identified grain properties and the proposed modeling methodology.

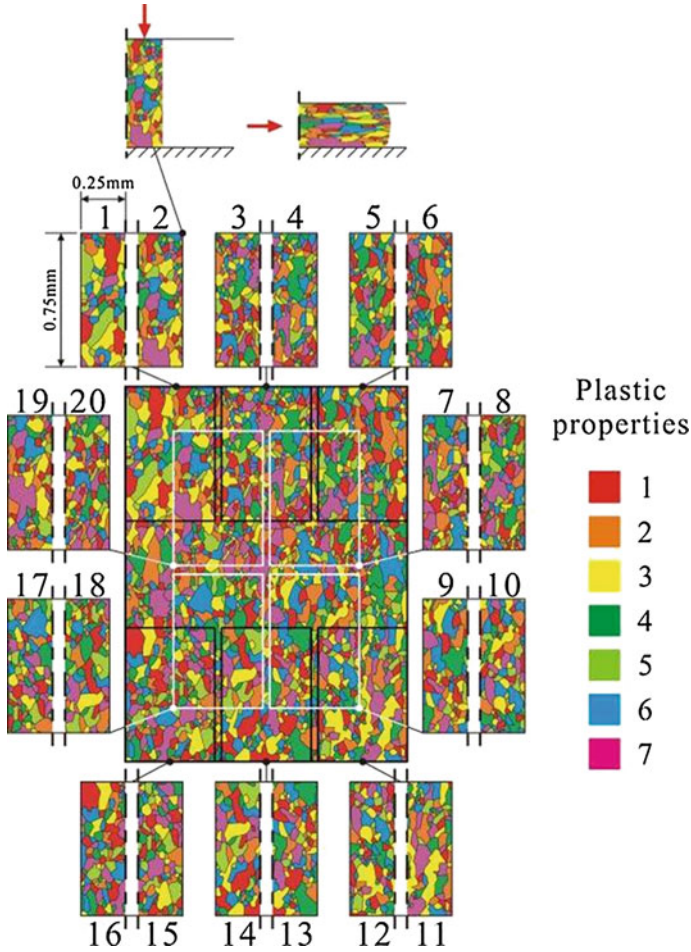


Fig. 2.37 The selected 20 cases for simulation of the compression of specimens with the D/d ratio of 12.5 [82]

2.4 Fracture Behavior

2.4.1 Fracture Strain and Fractograph

In microforming process, material undergoes large deformation which could lead to ductile fracture. Ductile fracture is one of the common defects in metal-formed parts caused by the tensile stress exceeding the strength limit of material. Controlling the amount and uniformity of deformation in each forming operation is critical to avoid fracture. Figure 2.47 shows the change of fracture strain with the variation of the ratio of testing foil thickness to grain size (t/d) in tensile test. It can

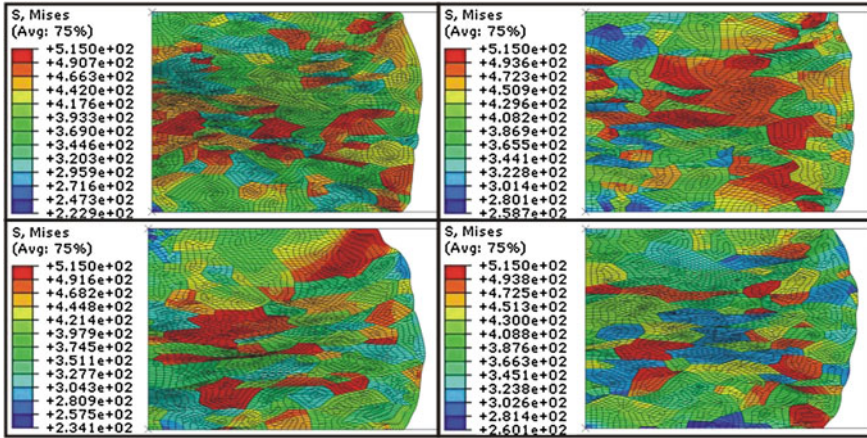
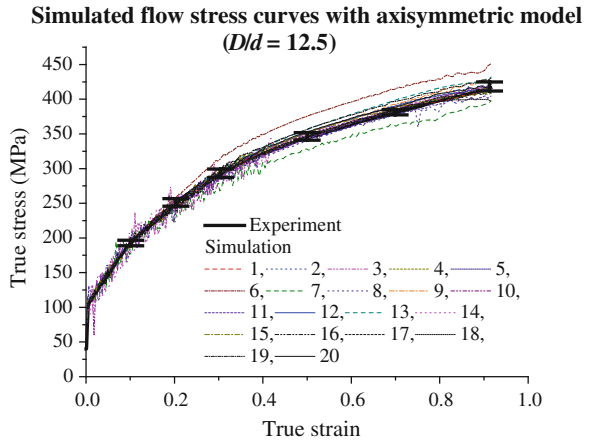


Fig. 2.38 The simulated stress distributions in the 2D axisymmetric models with the D/d ratio of 12.5 [82]

Fig. 2.39 The simulated flow stress curves in the axisymmetric models with the D/d ratio of 12.5 [82]



be seen that the fracture strain decreases with the number of grains over the foil thickness. Figure 2.48 shows the fractographs of the tested samples with the thickness of 600 and 100 μm , and the different values of t/d . It reveals the ductile fracture mode of the samples.

By comparing the fractographs of the samples with the same thickness (600 μm), as shown in Fig. 2.48a, b, it is found that the number of micro-voids decreases with t/d . In the extreme case with only about one grain ($t/d = 1.2$) in the thickness direction, there is no micro-void found and the slip band and the typical knife edge rupture can be clearly observed on the fracture surface, as shown in Fig. 2.48c. The decrease of t/d leads to the localized deformation at the fracture region. Actually, the measured strain is not the fracture strain at the fracture region,

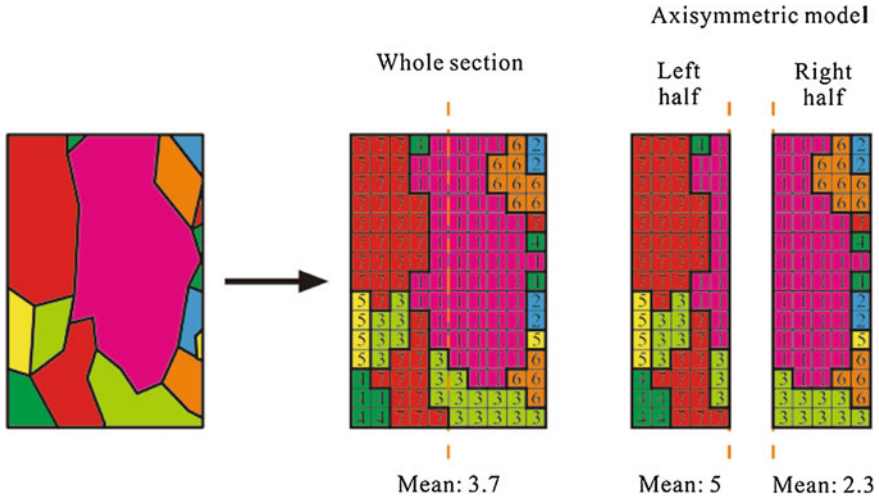


Fig. 2.40 Over- and under-estimation of mean flow stress in an axisymmetric model [82]

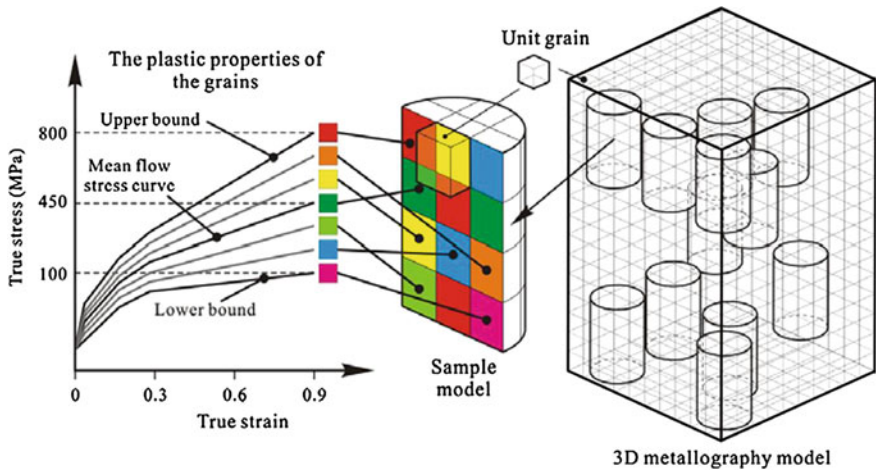


Fig. 2.41 Schematic illustration of the 3D full-scale model with cubic grain [82]

but it is the averaged strain over the gauge length. The decrease of fracture strain with the decreasing t/d could be attributed to the inhomogeneous deformation and the nonuniform distribution of plastic strain along the gauge length. It causes a significantly large strain localized at the fracture region [63]. The similar result of the nonuniform plastic strain in the coarse-grained material in microbending test is

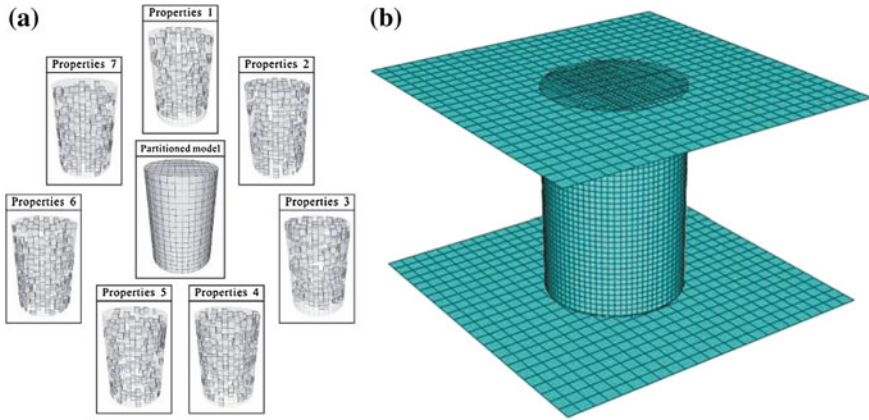


Fig. 2.42 FE model in the case with the D/d ratio of 12.5 [82]. **a** Partitioned model and **b** meshed model

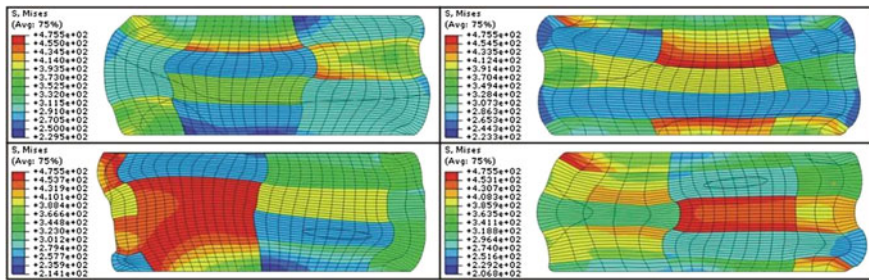


Fig. 2.43 The simulated stress distribution in the 3D full-scale models with the D/d ratio of 2.8 [82]

also reported in prior studies [64]. This could be attributed to the fact that the location, size, and orientation of the individual grains affect the deformation behavior significantly when the grain size approaches the specimen size.

In addition to the aforementioned explanation, the testing samples underwent rolling and electrical discharge machining processes. Surface flaws might be originated from these processes and the size of flaws is not scaled down with the thickness of specimen. It can be seen in Fig. 2.49 that the surface flaw at the side surface of the tested samples, which is induced in the electrical discharge machining process, becomes significant when the specimen thickness is decreased from 600 to 100 μm . The flaw acts as a stress-raiser leading to premature localized strain and early fracture [65]. Furthermore, when the specimen thickness is in the order of grain size or even smaller, it may perform like a single crystal with less constraint with neighboring grains. Only a few slip systems are activated to realize deformation, it would also result in small fracture strain [66].

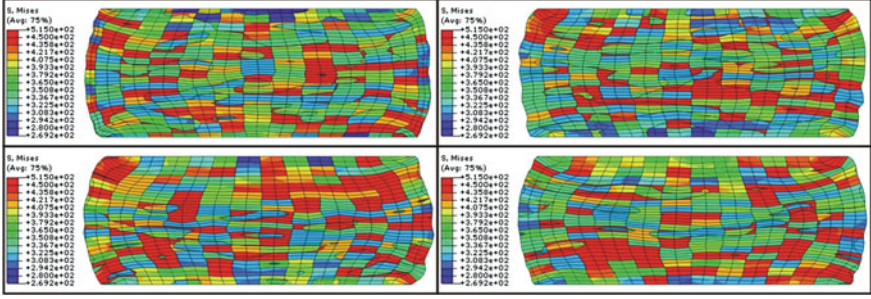
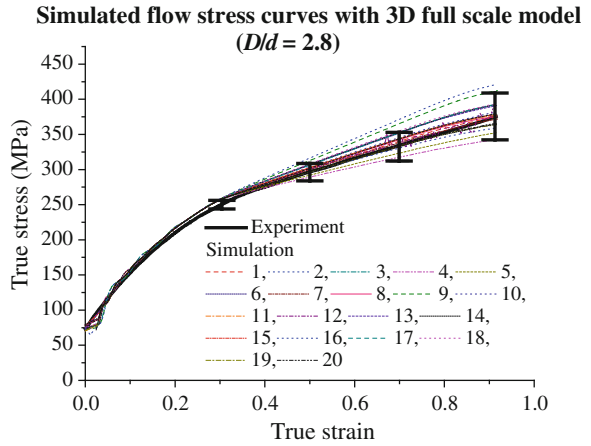


Fig. 2.44 The simulated stress distributions in the 3D full-scale models with the D/d ratio of 12.5 [82]

Fig. 2.45 The simulated flow curves in the 3D full-scale models with the D/d ratio of 2.8 [82]



2.4.2 Grain Statistics

Pure copper has the FCC crystal structure with 12 slip systems $\{111\} \langle 110 \rangle$. In the case that the grain is subject to uniaxial loading, the work increment (dw) by the slips in all the activated slip systems within a grain is

$$dw = \tau_c \sum_n |d\gamma_n| = \sigma_x d\epsilon_x \quad (2.35)$$

where the critical resolved shear stress (τ_c) is the same in all the slip systems and $d\gamma_n$ is the incremental slip in the n th slip system. The Taylor factor (m) which depends on the grain orientation is given by

$$m = \frac{\sigma_x}{\tau_c} = \frac{\sum_n |d\gamma_n|}{d\epsilon_x} \quad (2.36)$$

Fig. 2.46 The simulated flow stress curves in the 3D full-scale models with the D/d ratio of 12.5 [82]

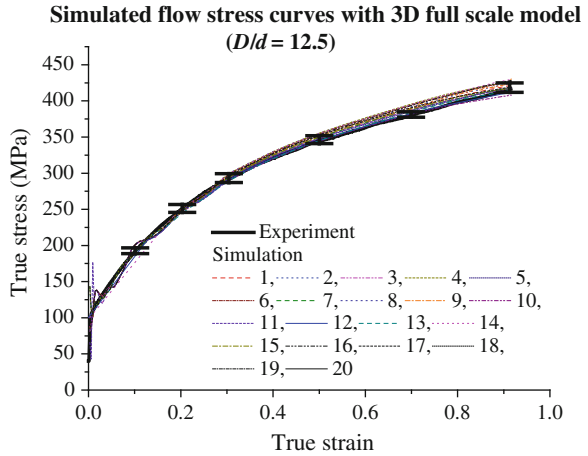
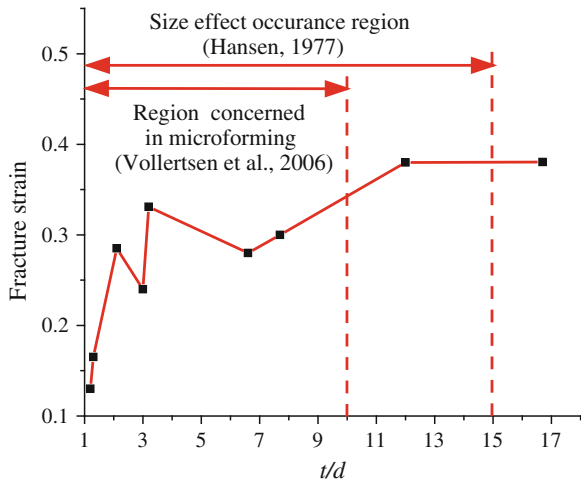


Fig. 2.47 Variation of fracture strain with t/d [83]



The Taylor factor can be represented in terms of von Misses stress (σ_v) and strain (ϵ_v) in the multiaxial stress state in the following:

$$m = \frac{\sigma_v}{\tau_c} = \frac{\sum_n |d\gamma_n|}{d\epsilon_v} = \frac{dw}{\tau_c d\epsilon_v} = \frac{\sigma : d\epsilon}{\tau_c d\epsilon_v} \tag{2.37}$$

The averaged Taylor factor is commonly used to represent the ratio of the macroscopic flow stress to the critical resolved shear stress for polycrystalline materials. This is based on the assumption that the soft grains cannot deform unless the hard and soft grains deform simultaneously and the shape change performs in the way of minimizing energy consumption, i.e., $\min\{dw\} = \tau_c \left[\min \left\{ \sum_n |d\gamma_n| \right\} \right]$. In the tensile test, plastic deformation begins when the local yield stress is reached.

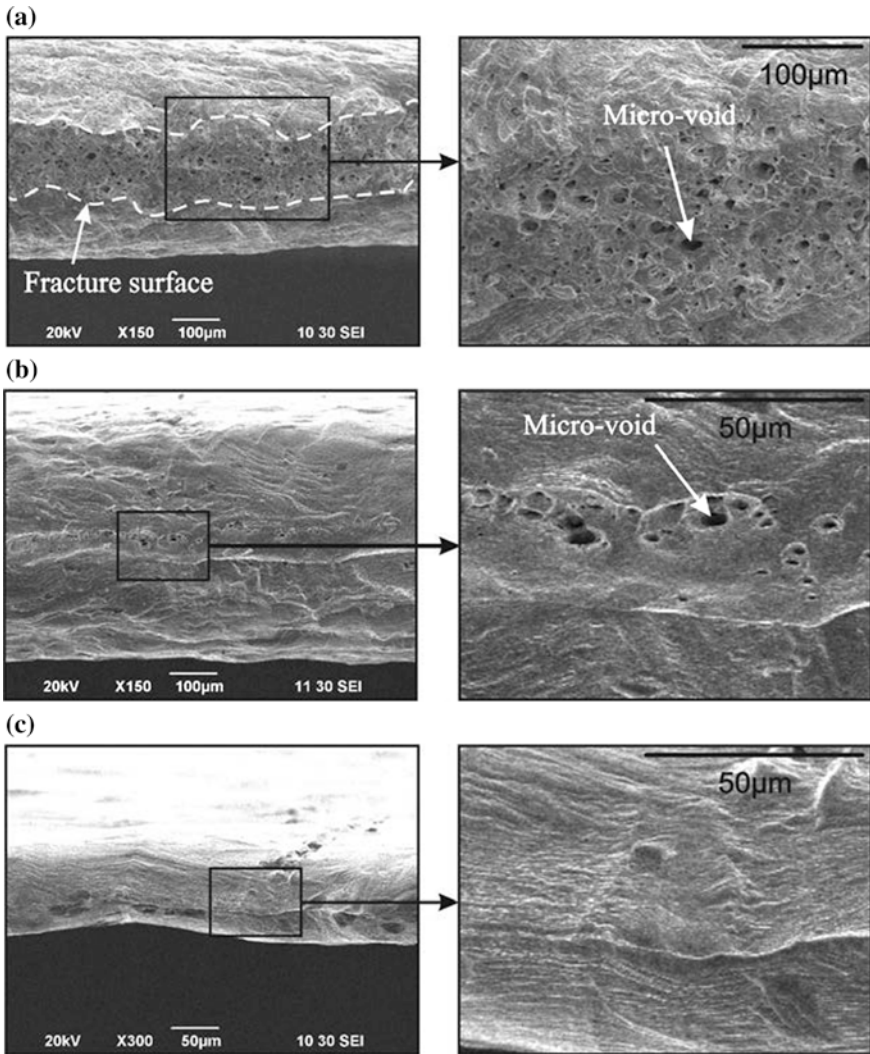


Fig. 2.48 Fractographs of the tested samples [83]. **a** $t = 600 \mu\text{m}$, $d = 36 \mu\text{m}$, $t/d = 16.7$, **b** $t = 600 \mu\text{m}$, $d = 286 \mu\text{m}$, $t/d = 2.1$ and **c** $t = 100 \mu\text{m}$, $d = 83 \mu\text{m}$, $t/d = 1.2$

The testing specimen can be considered as a chain illustrated in Fig. 2.50. Each specimen section perpendicular to the loading direction acts as a link member. The section of specimen yields when all the grains in that section yield. The initial yielding occurs at the weakest section [67]. The yield stress of the j th section is

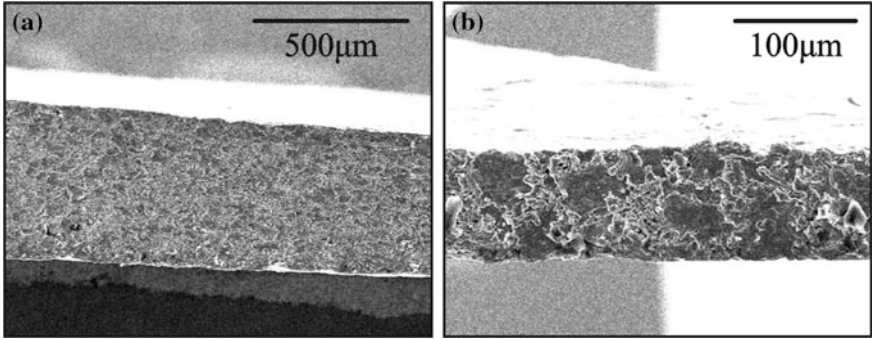
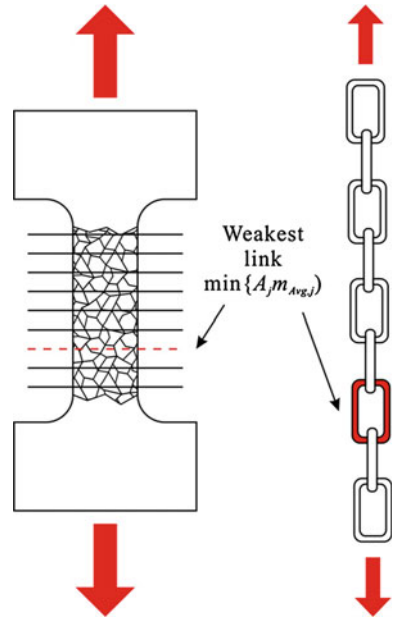


Fig. 2.49 The side surface of the tested samples [83]. **a** $t = 600 \mu\text{m}$ and **b** $t = 100 \mu\text{m}$

Fig. 2.50 Schematic illustration of yielding at the weakest section in the tensile testing specimen [84]

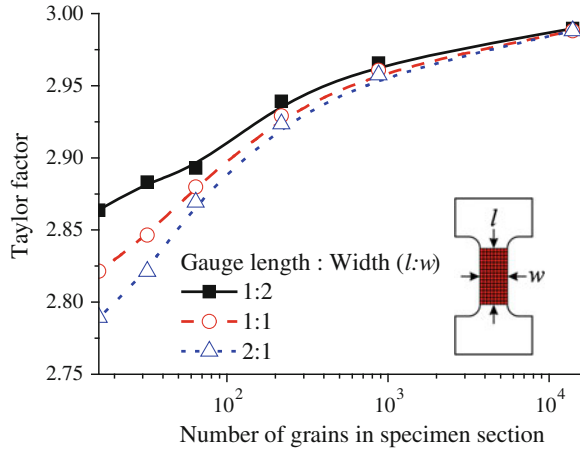


$$\sigma_j = \sum_i \sigma_{G,i} a_{i,j} = \tau_c \sum_i m_i a_{i,j} = \tau_c m_{Avg,j} \tag{2.38}$$

where $\sigma_{G,i}$, $a_{i,j}$ and m_i are the yield stress, area fraction and the Taylor factor of the i th grain in the j th section, respectively. $m_{Avg,j}$ is the averaged Taylor factor in the j th section. The force applied in the j th section is

$$F_j = \sigma_j A_j = \tau_c m_{Avg,j} A_j \tag{2.39}$$

Fig. 2.51 Change of the minimum Taylor factor ($\min\{m_{\text{Avg},j}\}$) in the tensile testing specimen [84]

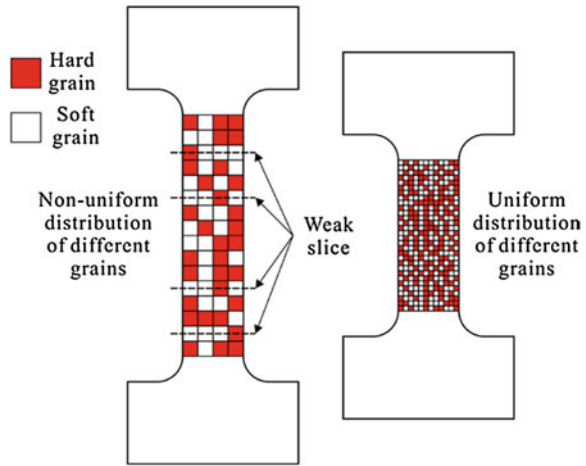


where A_j is the j th section area. The weakest section should be the one with $\min\{m_{\text{Avg},j} A_j\}$. In the testing specimen, the grains with the favorable orientation to deform along the loading direction could be considered as a soft portion, while other grains with the unfavorable orientation are considered as a hard portion. Minimization of plastic work can be achieved by selecting the specimen section with the smallest yield stress.

Based on the above analysis, simulation can be conducted to study the grain and specimen size effects on material yielding behavior. To simplify the model, it is assumed that the grain geometry in the specimen can be represented as a cubic and the cross-section area is the same in each section. Therefore, it is not necessary to consider different area fractions of different grains in each section and the weakest section is the one with the lowest averaged Taylor factor ($\min\{m_{\text{Avg},j}\}$). The Taylor factor of grain ranging from 2.3 to 3.7 [68] is given by a random number generator to model the random characteristic of grain properties. Fifty samples are modeled for each case with a specified number of grains in the specimen section and the ratio of gauge length to specimen width.

The change of $\min\{m_{\text{Avg},j}\}$ with different numbers of grains in the specimen section and different gauge lengths is simulated and the mean values are presented in Fig. 2.51. It can be seen that the $\min\{m_{\text{Avg},j}\}$ decreases with the number of grains in the specimen section. It has a good correlation with the experimental results on the change of flow stress and fracture strain. In addition, the $\min\{m_{\text{Avg},j}\}$ increases with the decrease of gauge length. The simulation results suggest that the longer gauge length and the smaller number of grains in the specimen section, the higher probability to have a section with a significantly large fraction of soft grains, as illustrated in Fig. 2.52. This could be due to the fact that the distribution of different grains becomes nonuniform when there are only a few grains constituting the specimen. A significant large deformation could be concentrated at the soft grains. This further leads to the small fracture strain in the tensile test.

Fig. 2.52 Grain and specimen size effects on the distribution of different grains [84]



2.5 Elastic Recovery

In development of microscale parts, the control of geometrical accuracy of the micro-formed parts is a critical issue as the requirement of dimension accuracy with less than a few microns is always needed in many industrial clusters. The springback caused by the elastic recovery affects the dimensional accuracy of the micro-formed parts. Fu et al. [69] investigated the springback behavior in the leadframe production process based on L-bending. It is revealed that the springback increases with die radius, die angle, and the punch-die clearance. In addition, it is found that the strip along the rolling direction exhibits a larger springback than that of the transverse direction. Liu et al. [15] conducted the three point bending tests using copper foils to study the interactive effect of specimen and grain sizes. It is found that the springback increases with the decreasing ratio of specimen thickness to grain size, as shown in Fig. 2.53a. The similar result obtained by using brass foils is also reported by Gau et al. [28]. Diehl et al. [70] investigated the size effect on the springback based on L-bending using different size-scaled pure copper foils with similar microstructure. It is found that the springback decreases with foil thickness when the influence of surface grain dominates, as shown in Fig. 2.53b. When the foil thickness is decreased to a certain value, the strain gradient effect takes place and the amount of springback increases with the decrease of foil thickness.

2.6 Surface Roughening

The interaction of deformation among surface grains with different orientations makes the formed micropart surface rough. Figure 2.54 shows the SEM images of the surface topographies of the compressed copper cylinders captured under the

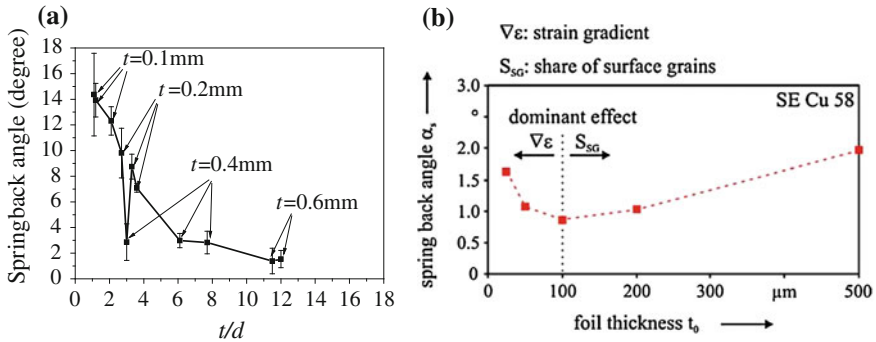


Fig. 2.53 Change of springback angle with the variation of specimen thickness and grain size [15, 70]. **a** 3-point bending and **b** L-bending

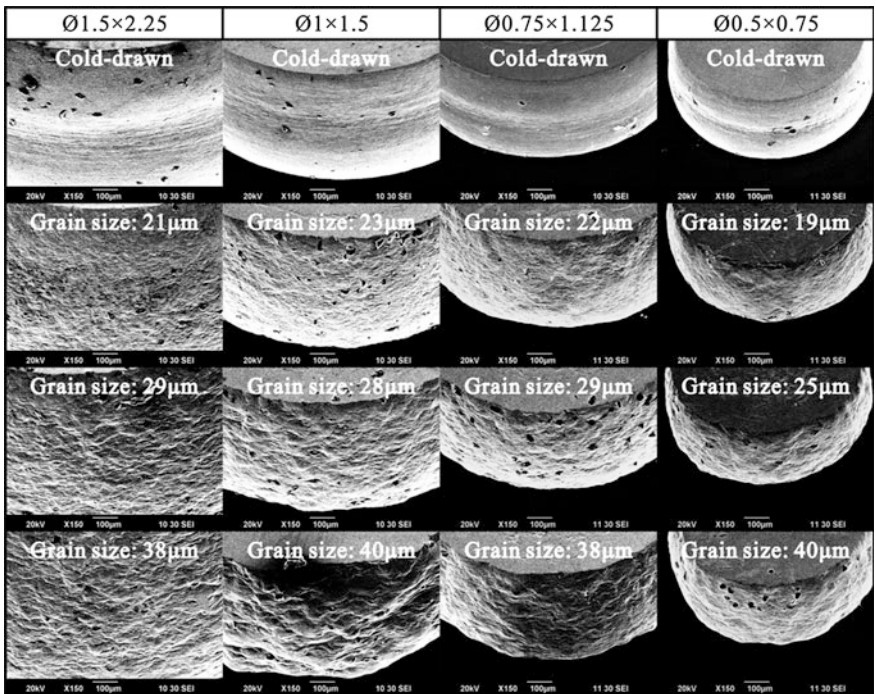


Fig. 2.54 Surface topographies of the compressed specimens [21]

same magnification ratio. It can be seen that the surface roughness increases with the grain size in different size-scaled samples, while roughening does not occur in the cold-drawn samples. Quantitative evaluation on this size effect can be done via the measurement of the surface roughnesses of the elongated foils with different

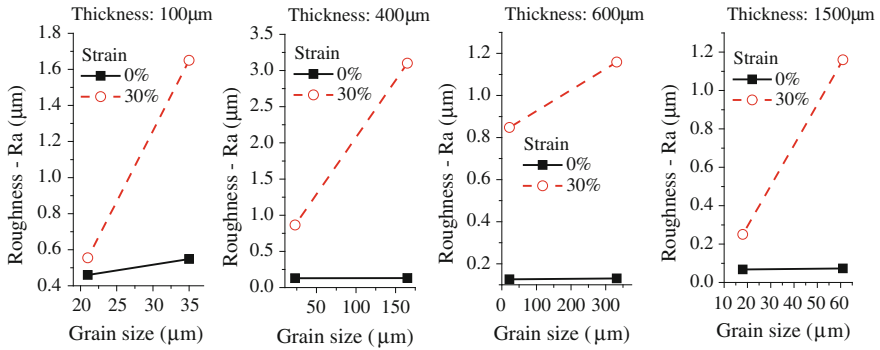
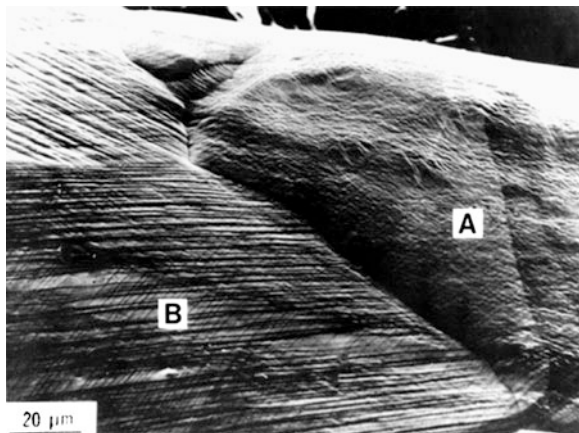


Fig. 2.55 Change of surface roughness with strain and grain size for a given specimen thickness [71]

Fig. 2.56 Scanning electron micrograph of the deformed aluminum polycrystal. Well-defined slip bands occur in all the grains except grain A. Three slip line systems are present in grain B [85]



thicknesses and grain sizes using profilometer [71]. The measured surface roughnesses are shown in Fig. 2.55. The similar experimental results of the increase of surface roughness with the increasing amount of deformation and grain size can also be found in other studies using steels and aluminum alloys [72, 73].

Grain deformation mechanisms have a close relationship with surface roughening. Grains deform via slip in the particular systems and the neighboring grains have different crystallographic orientations. This results in strain incompatibility between neighboring grains and different amount of deformation in different grains [74]. The surface grains have less constraint so that the strain incompatibility make the grains move normal to the surface. In addition, deformation is generally restricted near the grain boundaries, which leads to the formation of grooves, as shown in Fig. 2.56. The formation of grooves was investigated by Urie and Wain [75] through the measurement of local elongation in the individual grains of

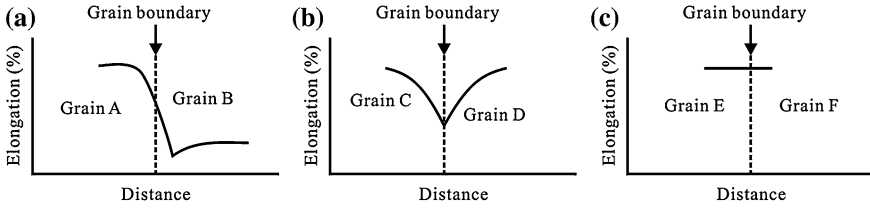


Fig. 2.57 Schematics of three types of elongation curves near grain boundary [75]

aluminum. The deformation behaviors in the vicinity of grain boundary can be classified into three categories schematically illustrated in Fig. 2.57. The most common type is that the average deformation on either side of the boundary is quite different. Relatively large deformation only takes place inside one of the grains shown in Fig. 2.57a. The other two types of deformation behaviors occur when the amount of deformation in both grains is almost the same. In one scenario, there is a considerable restriction in deformation at the grain boundary as shown in Fig. 2.57b, while the other scenario is that the boundary has only a subtle influence on the deformation presented in Fig. 2.57c.

On the other hand, there is no surface roughening effect in the cold-drawn material, as shown in Fig. 2.54. This can be explained based on the fine microstructure and the strong crystallographic texture that the strain incompatibility among grains is not significant [76–79]. In addition, surface roughening effect is also related to crystal structure [80]. Greater roughening effect occurs for the crystal structure with few available slip systems, such as HCP. This can be ascribed to the fact that only a few slip systems accommodate local deformation, resulting in the increase of strain incompatibility. Based on the above-reported results, it can be found that the surface roughening effect has a close correlation with the specimen size, grain size, crystallographic texture, and crystal structure. A rough surface can cause strain localization, lower forming limit, increase tooling-workpiece interface friction, and weaken the mechanical properties of the formed microparts. The surface roughening effect thus needs to be taken into account in design of microforming system and the quality control and assurance of microparts.

2.7 Summary

The conventional knowledge in macro-scaled forming processes is not fully valid or effective to support the design and development of microparts via microforming due to the occurrence of different size effects with the decrease of part or part feature size. Size effects significantly affect the quality of micro-formed part in terms of dimensional accuracy, surface finishing and mechanical properties.

Understanding of the size effect-related deformation behaviors and phenomena and size effect mechanisms is crucial in micropart development via microforming.

It is known that grain boundary increases the strength of material via blocking the movement of dislocations. The ratio of the total grain boundary surface area to material volume decreases with the decrease of specimen size and the increase of grain size. This leads to the decrease of grain boundary strengthening effect. In addition, surface grains have less constraint compared to internal grains. The change of flow stress with part geometry size is partly attributed to the change of volume fraction of surface grains. Regarding the size effect on deformation behavior, even distribution of different grains no longer exists when there are only a few grains in the microscale workpiece. The anisotropic properties of each grain and the random nature of grain distribution and orientation become significant, which lead to the inhomogeneous deformation, irregular-formed geometry, and the scatter of the measured flow stress and other deformation-related variables.

Based on the tensile test results, fracture strain decreases with the ratio of specimen size to grain size. The distribution of plastic strain becomes nonuniform along the gauge length when there are only a few grains in the cross-section of specimen. This leads to a large strain localized at the grains which are favorable to deform in tensile direction. There is an interactive effect of the grain and specimen sizes on deformation behavior in tensile test. The measured data in tensile test could be significantly affected by individual grains along the gauge length. Therefore, the accuracy of the measured data needs to be examined.

The anisotropic properties of grain and the incompatibility among the neighboring grains at the free surface lead to the grains moving normal to the material surface in deformation process. In addition, the deformation at grain boundary region is restricted, resulting in the formation of groove. The above issues further make the surface of the deformed material rough. When the formed part size is decreased to microscale and the grain size is large, the surface roughening effect could significantly lower the formability of material and the dimensional accuracy of the formed part.

Although the polycrystalline material deformation behaviors have been extensively studied, the physics behind the size effect is not yet thoroughly understood. Nowadays, the size effect in microforming processes is still a challenging issue to be explored. This chapter presents the understanding and knowledge of size effects and the size effect-affected deformation behaviors, which help the design and development of microparts via microforming.

References

1. Engel U, Eckstein R (2002) Microforming—from basic research to its realization. *J Mater Process Technol* 125:35–44
2. Chan WL, Fu MW, Lu J, Chan LC (2009) Simulation-enabled study of folding defect formation and avoidance in axisymmetrical flanged components. *J Mater Process Technol* 209(11):5077–5086

3. Chan WL, Fu MW, Lu J (2010) FE simulation-based folding defect prediction and avoidance in forging of axially symmetrical flanged components. *J Manuf Sci Eng Trans ASME* 132(5)
4. Fu MW, Li H, Lu J, Lu SQ (2009) Numerical study on the deformation behaviors of the flexible die forming by using viscoplastic pressure-carrying medium. *Comput Mater Sci* 46(4):1058–1068
5. Fu MW, Lu J, Chan WL (2009) Die fatigue life improvement through the rational design of metal-forming system. *J Mater Process Technol* 209(2):1074–1084
6. Fu MW, Yong MS, Tong KK, Muramatsu T (2006) A methodology for evaluation of metal forming system design and performance via CAE simulation. *Int J Prod Res* 44(6):1075–1092
7. Vollertsen F, Biermann D, Hansen HN, Jawahir IS, Kuzman K (2009) Size effects in manufacturing of metallic components. *Cirp Ann Manuf Technol* 58(2):566–587
8. Messner A, Engel U, Kals R, Vollertsen F (1994) Size effect in the Fe-simulation of micro-forming processes. *J Mater Process Technol* 45(1–4):371–376
9. Vollertsen F, Hu Z, Niehoff HS, Theiler C (2004) State of the art in micro forming and investigations into micro deep drawing. *J Mater Process Technol* 151(1–3):70–79
10. Geiger M, Vollertsen F, Kals R (1996) Fundamentals on the manufacturing of sheet metal microparts. *CIRP Ann Manuf Technol* 45(1):277–282
11. Geiger M, Meßner A, Engel U (1997) Production of microparts—size effects in bulk metal forming, similarity theory. *Prod Eng Res Devel* 4(1):55–58
12. Barbier C, Thibaud S, Richard F, Picart P (2009) Size effects on material behavior in microforming. *Int J Mater Form* 2:625–628
13. Raulea LV, Govaert LE, Baaijens FPT (1999) Grain and specimen size effects in processing metal sheets. In: *Sixth international conference on technology of plasticity*. Springer, Nuremberg
14. Chen FK, Tsai JW (2006) A study of size effect in micro-forming with micro-hardness tests. *J Mater Process Technol* 177(1–3):146–149
15. Liu JG, Fu MW, Lu J, Chan WL (2011) Influence of size effect on the springback of sheet metal foils in micro-bending. *Comput Mater Sci* 50(9):2604–2614
16. Chan WL, Fu MW, Lu J (2011) The size effect on micro deformation behaviour in micro-scale plastic deformation. *Mater Des* 32(1):198–206
17. Vollertsen F, Niehoff HS, Hu Z (2006) State of the art in micro forming. *Int J Mach Tools Manuf* 46(11):1172–1179
18. Meyers MA, Ashworth E (1982) A Model for the Effect of Grain-Size on the Yield Stress of Metals. *Phil Mag Phys Condens A Matter Struct Defects Mech Prop* 46(5):737–759
19. Kim GY, Ni J, Koc M (2007) Modeling of the size effects on the behavior of metals in microscale deformation processes. *J Manuf Sci Eng Trans ASME* 129(3):470–476
20. Mahabunphachai S, Koc M (2008) Investigation of size effects on material behavior of thin sheet metals using hydraulic bulge testing at micro/meso-scales. *Int J Mach Tools Manuf* 48(9):1014–1029
21. Chan WL, Fu MW, Yang B (2012) Experimental studies of the size effect affected microscale plastic deformation in micro upsetting process. *Mater Sci Eng A* 534:374–383
22. Hug E, Keller C (2010) Intrinsic Effects due to the Reduction of Thickness on the Mechanical Behavior of Nickel Polycrystals. *Metall Mater Trans A Phys Metall Mater Sci* 41A(10):2498–2506
23. Petch NJ (1953) The cleavage strength of polycrystals. *J Iron Steel Inst* 174(1):25–28
24. Hall EO (1951) The deformation and ageing of mild Steel III—discussion of results. *Proc Phys Soc London Sect B* 64(381):747–753
25. Armstrong R, Douthwaite RM, Codd I, Petch NJ (1962) Plastic deformation of polycrystalline aggregates. *Phil Mag* 7(73):45–58
26. Gau JT, Principe C, Wang JW (2007) An experimental study on size effects on flow stress and formability of aluminum and brass for microforming. *J Mater Process Technol* 184(1–3):42–46

27. Miyazaki S, Shibata K, Fujita H (1979) Effect of specimen thickness on mechanical-properties of polycrystalline aggregates with various grain sizes. *Acta Metall* 27(5):855–862
28. Gau JT, Principe C, Yu M (2007) Springback behavior of brass in micro sheet forming. *J Mater Process Technol* 191(1–3):7–10
29. Hansen N (2005) Boundary strengthening over five length scales. *Adv Eng Mater* 7(9):815–821
30. Chan WL, Fu MW (2012) Studies of the interactive effect of specimen and grain sizes on the plastic deformation behavior in microforming. *Int J Adv Manuf Technol* 62(9):989–1000
31. Hirth JP (1972) Influence of grain-boundaries on mechanical properties. *Metall Trans* 3(12):3047–3067
32. Mecking H (1979) Deformation of polycrystals. In: Haasen P, Gerold V, Kosterz G (eds) *Proceedings of the 5th international conference on the strength of metals and alloys, 1979, Aachen, Federal Republic of Germany*, Pergamon, pp 1573–1594
33. Feaugas X (1999) On the origin of the tensile flow stress in the stainless steel AISI 316L at 300 K: Back stress and effective stress. *Acta Mater* 47(13):3617–3632
34. Kocks UF (1976) Laws for Work-Hardening and Low-Temperature Creep. *J Eng Mater Technol Trans ASME* 98(1):76–85
35. Kocks UF (1970) Relation between polycrystal deformation and single-crystal deformation. *Metall Trans* 1(5):1121–1143
36. Voigt W (1889) Ueber die Beziehung zwischen den beiden Elasticitätsconstanten isotroper Körper. *Ann Phys* 274(12):573–587
37. Benson DJ, Fu HH, Meyers MA (2001) On the effect of grain size on yield stress: extension into nanocrystalline domain. *Mater Sci Eng A Struct Mater Prop Microstruct Process* 319:854–861
38. Fu HH, Benson DJ, Meyers MA (2001) Analytical and computational description of effect of grain size on yield stress of metals. *Acta Mater* 49(13):2567–2582
39. Van Swygenhoven H, Spaczer M, Caro A (1999) Microscopic description of plasticity in computer generated metallic nanophase samples: a comparison between Cu and Ni. *Acta Mater* 47(10):3117–3126
40. Gleiter H (2000) Nanostructured materials: basic concepts and microstructure. *Acta Mater* 48(1):1–29
41. Schiøtz J, Di Tolla FD, Jacobsen KW (1998) Softening of nanocrystalline metals at very small grain sizes. *Nature* 391(6667):561–563
42. Kim HS (1998) A composite model for mechanical properties of nanocrystalline materials. *Scripta Mater* 39(8):1057–1061
43. Carsley JE, Ning J, Milligan WW, Hackney SA, Aifantis EC (1995) A simple, mixtures-based model for the grain-size dependence of strength in nanophase metals. *Nanostruct Mater* 5(4):441–448
44. Zhou JQ, Li ZH, Zhu RT, Li YL, Zhang ZZ (2008) A mixtures-based model for the grain size dependent mechanical behavior of nanocrystalline materials. *J Mater Process Technol* 197(1–3):325–336
45. Drucker DC (1950) Some implications of work hardening and ideal plasticity. *Q Appl Math* 7:411–418
46. Donovan PE (1989) A yield criterion for Pd40Ni40P20 metallic glass. *Acta Metall* 37(2):445–456
47. Jiang B, Weng GJ (2004) A generalized self-consistent polycrystal model for the yield strength of nanocrystalline materials. *J Mech Phys Solids* 52(5):1125–1149
48. Jiang B, Weng GJ (2004) A theory of compressive yield strength of nano-grained ceramics. *Int J Plast* 20(11):2007–2026
49. Reuss A (1929) Berechnung der Fließgrenze von Mischkristallen auf Grund der Plastizitätsbedingung für Einkristalle. *ZAMM—J Appl Math Mech/Zeitschrift für Angewandte Mathematik und Mechanik* 9(1):49–58
50. Geiger M, Kleiner M, Eckstein R, Tiesler N, Engel U (2001) Microforming. *Cirp Annal Manuf Technol* 50(2):445–462

51. Kals R, Pucher HJ, Vollertsen F (1995) Effects of specimen size and geometry in metal forming. In: 2nd international conference on advances in materials and processing technologies, Dublin
52. Shen Y, Yu HP, Ruan XY (2006) Discussion and prediction on decreasing flow stress scale effect. *Trans Nonferrous Metal Soc China* 16(1):132–136
53. Peng LF, Lai XM, Lee HJ, Song JH, Ni J (2009) Analysis of micro/mesoscale sheet forming process with uniform size dependent material constitutive model. *Mater Sci Eng A Struct Mater Prop Microstruct Process* 526(1–2):93–99
54. Peng LF, Liu F, Ni J, Lai XM (2007) Size effects in thin sheet metal forming and its elastic-plastic constitutive model. *Mater Des* 28(5):1731–1736
55. Lai XM, Peng LF, Hu P, Lan SH, Ni J (2008) Material behavior modelling in micro/meso-scale forming process with considering size/scale effects. *Comput Mater Sci* 43(4):1003–1009
56. Schmid E, Boas W (1968) *Plasticity of crystals, with special reference to metals*. Chapman and Hall, London, p 353
57. Sachs G (1928) Zur Ableitung einer Fließbedingung. *Zeichschrift Ver Dtsch Ing* 72:734–736
58. Taylor GI (1938) Plastic strains in metals. *J Inst Met* 62:307–324
59. Kocks UK, Canova GR (1981) How many slip systems, and which? In: 2nd Risø international symposium on metallurgy and materials science. Risø National Laboratory, Denmark
60. Leffers T (1981) Microstructures and mechanisms of polycrystal deformation at low temperature. In: 2nd Risø international symposium on metallurgy and materials science. Risø National Laboratory, Denmark
61. Eichenhueller B, Egerer E, Engel U (2007) Microforming at elevated temperature—forming and material behaviour. *Int J Adv Manuf Technol* 33(1–2):119–124
62. Egerer E, Engel U (2004) Process characterization and material flow in microforming at elevated temperatures. *J Manuf Process* 6(1):1–6
63. Simons G, Weippert C, Dual J, Villain J (2006) Size effects in tensile testing of thin cold rolled and annealed Cu foils. *Mater Sci Eng A Struct Mater Prop Microstruct Process* 416(1–2):290–299
64. Parasiz SA, VanBenthysen R, Kinsey BL (2010) Deformation size effects due to specimen and grain size in microbending. *J Manuf Sci Eng Trans ASME* 132(1):011018
65. Ebrahimi F, Ahmed Z, Li HQ (2006) Tensile properties of electrodeposited nanocrystalline FCC metals. *Mater Manuf Processes* 21(7):687–693
66. Klein M, Hadrboletz A, Weiss B, Khatibi G (2001) The ‘size effect’ on the stress-strain, fatigue and fracture properties of thin metallic foils. *Mater Sci Eng A Struct Mater Prop Microstruct Process* 319:924–928
67. Henning M, Vehoff H (2007) Statistical size effects based on grain size and texture in thin sheets. *Mater Sci Eng A Struct Mater Prop Microstruct Process* 452:602–613
68. Chin GY, Mammel WL (1967) Computer solutions of the Taylor analysis for axisymmetric flow. *Trans TMS-AIME* 239:1400–1405
69. Fu MH, Chan KC, Lee WB, Chan LK (1997) Springback in the roller forming of integrated circuit leadframes. *J Mater Process Technol* 66(1–3):107–111
70. Diehl A, Engel U, Geiger M (2010) Influence of microstructure on the mechanical properties and the forming behaviour of very thin metal foils. *Int J Adv Manuf Technol* 47(1–4):53–61
71. Chan WL, Fu MW (2012) Experimental studies of plastic deformation behaviors in microheading process. *J Mater Process Technol* 212(7):1501–1512
72. Chen GN, Shen H, Hu SU, Baudelet B (1990) Roughening of the free surfaces of metallic sheets during stretch forming. *Mater Sci Eng A Struct Mater Prop Microstruct Process* 128(1):33–38
73. Chandrasekaran D, Nygard M (2003) A study of the surface deformation behaviour at grain boundaries in an ultra-low-carbon steel. *Acta Mater* 51(18):5375–5384

74. Bretheau T, Caldemaison D (1981) Test of mechanical interaction models between polycrystal grains by means of local strain measurements. In: 2nd Risø international symposium on metallurgy and materials science. Risø National Laboratory, Denmark
75. Urie VM, Wain HL (1952) Plastic deformation of coarse-grained aluminum. *J Inst Met* 81:153–159
76. Beaudoin AJ, Acharya A, Chen SR, Korzekwa DA, Stout MG (2000) Consideration of grain-size effect and kinetics in the plastic deformation of metal polycrystals. *Acta Mater* 48(13):3409–3423
77. Hurley PJ, Humphreys FJ (2003) The application of EBSD to the study of substructural development in a cold rolled single-phase aluminium alloy. *Acta Mater* 51(4):1087–1102
78. Wu PD, Lloyd DJ (2004) Analysis of surface roughening in AA6111 automotive sheet. *Acta Mater* 52(7):1785–1798
79. Wilson DV, Roberts WT, Rodrigues PMB (1981) Effects of Grain Anisotropy on Limit Strains in Biaxial Stretching .2. Sheets of cubic metals and alloys with well-developed preferred orientations. *Metall Trans A Phys Metall Mater Sci* 12(9):1603–1611
80. Osakada K, Oyane M (1971) On the roughening of free surface in deformation processes. *Bull Jpn Soc Mech Eng* 14(68):171–177
81. Chan WL, Fu MW (2011) Experimental studies and numerical modeling of the specimen and grain size effects on the flow stress of sheet metal in microforming. *Mater Sci Eng A* 528(25–26):7674–7683
82. Chan WL, Fu MW, Lu J, Liu JG (2010) Modeling of grain size effect on micro deformation behavior in micro-forming of pure copper. *Mater Sci Eng A* 527(24–25):6638–6648
83. Fu MW, Chan WL (2011) Geometry and grain size effects on the fracture behavior of sheet metal in micro-scale plastic deformation. *Mater Des* 32(10):4738–4746
84. Chan WL, Fu MW (2012) Experimental and simulation based study on micro-scaled sheet metal deformation behavior in microembossing process. *Mater Sci Eng A* 556:60–67
85. Barlow CYJ, Bay B, Hansen N (1985) A comparative investigation of surface relief structures and dislocation microstructures in cold-rolled aluminum. *Philos Mag A Phys Condens Matter Struct Defects Mech Prop* 51(2):253–275



<http://www.springer.com/978-1-4471-6325-1>

Micro-scaled Products Development via Microforming
Deformation Behaviours, Processes, Tooling and its
Realization

Fu, M.W.; Chan, W.L.

2014, XIII, 175 p. 191 illus., 131 illus. in color.,

Hardcover

ISBN: 978-1-4471-6325-1